Complex organic molecules towards the central molecular zone of NGC 253

Citation for the original published paper (version of record):

Bouvier, M., Viti, S., Mangum, J. et al (2025). Complex organic molecules towards the central molecular zone of NGC 253. Astronomy and Astrophysics, 698. http://dx.doi.org/10.1051/0004-6361/202554420

N.B. When citing this work, cite the original published paper.

(article starts on next page)

Astronomy & Astrophysics

Complex organic molecules towards the central molecular zone of NGC 253

M. Bouvier[1],⋆ , S. Viti[1,2,3] , J. G. Mangum[4] , C. Eibensteiner[4],⋆⋆ , E. Behrens[5,4] , V. M. Rivilla[6] ,
Á. López-Gallifa[6], S. Martín[7,8], N. Harada[9,10] , S. Muller[11] , L. Colzi[6] , and K. Sakamoto[12]

[1] Leiden Observatory, Leiden University, PO Box 9513, 2300 RA Leiden, The Netherlands
[2] Transdisciplinary Research Area (TRA) 'Matter'/Argelander-Institut für Astronomie, University of Bonn, Germany
[3] Physics and Astronomy, University College London, UK
[4] National Radio Astronomy Observatory, 520 Edgemont Road, Charlottesville, VA 22903-2475, USA
[5] Department of Astronomy, University of Virginia, PO Box 400325, 530 McCormick Road, Charlottesville, VA 22904-4325, USA
[6] Centro de Astrobiología (CAB), CSIC-INTA, Carretera de Ajalvir km 4, Torrejón de Ardoz, 28850 Madrid, Spain
[7] European Southern Observatory, Alonso de Córdova, 3107, Vitacura, Santiago 763-0355, Chile
[8] Joint ALMA Observatory, Alonso de Córdova, 3107, Vitacura, Santiago 763-0355, Chile
[9] National Astronomical Observatory of Japan, 2-21-1 Osawa, Mitaka, Tokyo 181-8588, Japan
[10] Department of Astronomy, School of Science, The Graduate University for Advanced Studies (SOKENDAI), 2-21-1 Osawa, Mitaka, Tokyo, 181-1855 Japan
[11] Department of Space, Earth and Environment, Chalmers University of Technology, Onsala Space Observatory, SE-43992 Onsala, Sweden
[12] Institute of Astronomy and Astrophysics, Academia Sinica, 11F of AS/NTU Astronomy-Mathematics Building, No.1, Sec. 4, Roosevelt Rd, Taipei 106319, Taiwan

ABSTRACT

Context. Interstellar complex organic molecules (iCOMs) could be linked to prebiotic species, which are the key building blocks of life. In Galactic star-forming (SF) regions, spatial variations in iCOM emission could reflect the source's physical structure or different chemical formation pathways. Thus, investigating iCOMs in extragalactic SF regions can provide crucial information about these regions.

Aims. As an active extragalactic SF region, the central molecular zone (CMZ) of the nearby galaxy NGC 253 provides an ideal template for studying iCOMs under more extreme conditions. We aim to investigate the emission of a few selected iCOMs to understand whether a difference between the iCOMs could shed light on the source's chemical or physical structure.

Methods. Using high angular resolution (∼27 pc) observations from the ALCHEMI ALMA large programme, we imaged the emission of selected iCOMs and precursors; CH_3CHO, C_2H_5OH, NH_2CHO, CH_2NH, and CH_3NH_2. We estimated the gas temperatures and column densities of the iCOMs using a rotational diagram analysis, along with a non-local thermodynamic equilibrium (NLTE) analysis for CH_2NH.

Results. The iCOM emission is concentrated mainly towards the inner part of the CMZ of NGC 253 and it can be reproduced with two gas components. Different emission processes can explain iCOM emission towards the CMZ of NGC 253: at giant molecular cloud (GMC) scales (∼27 pc), the iCOMs could trace large-scale shocks; whilst at smaller scales (of only a few parsecs), both shock and heating processes linked with ongoing star formation could be involved. Using trends in the column density correlation and known formation pathways, we find that there might be more than one formation path involved to explain the iCOM emission. Finally, we found chemical differences between the GMCs, such as a decrease in abundance for the N-bearing species towards one of the GMCs and different excitation conditions for NH_2CHO and CH_3CHO towards two of the GMCs.

Key words. astrochemistry – methods: observational – ISM: molecules – galaxies: ISM – galaxies: starburst

1. Introduction

One of the key topics in astrochemistry is how complex species can form and survive under the harsh conditions of the interstellar medium (ISM); in particular, interstellar complex organic molecules (iCOMs), which are carbon-bearing molecules of at least six atoms (Herbst & van Dishoeck 2009; Ceccarelli et al. 2017). Other species that do not fit formally into this category are also relevant for prebiotic chemistry. This is the case of methanimine (CH_2NH), the simplest imine and an impor-

tant precursor of glycine (e.g. Theule et al. 2011; Danger et al. 2011). In particular, iCOMs have been of interest due to their potential in forming prebiotic molecules, which are the key building blocks of life. Within our Galaxy, iCOMs are particularly abundant in various star-forming (SF) regions (e.g. Blake et al. 1987; Herbst & van Dishoeck 2009; Belloche et al. 2019; Jørgensen et al. 2020; Ceccarelli et al. 2023; Chen et al. 2023) and our Galactic Centre (see e.g. Jimenez-Serra 2025 references therein). However, despite numerous observations, understanding iCOM formation pathways is challenging. Two main chemical paradigms have been invoked in the literature, namely: a grain-surface only synthesis and the combination of a

---

⋆ Corresponding author: bouvier@strw.leidenuniv.nl
⋆⋆ Jansky Fellow of the National Radio Astronomy Observatory.

grain-surface and gas-phase synthesis (see Ceccarelli et al. 2023 and references therein for a review).

Multiple observations of iCOMs in Galactic SF Regions, at both low and high angular resolution, revealed a dichotomy among iCOMs, in particular between O- and N-bearing species (e.g. Blake et al. 1987; Caselli et al. 1993; Widicus Weaver et al. 2017; Codella et al. 2017; Suzuki et al. 2018; Csengeri et al. 2019; Bøgelund et al. 2019a; van der Walt et al. 2021; Mininni et al. 2023; Peng et al. 2022; Busch et al. 2024; Bouscasse et al. 2024). The cause for this kind of apparent segregation between N-bearing and O-bearing species is not clear, but several hypotheses have been proposed. These include differences in thermal history (e.g. Caselli et al. 1993; Viti et al. 2004; Suzuki et al. 2018; Garrod et al. 2022) or in the formation and destruction pathways of the species (e.g. Busch et al. 2024), as well as in the intrinsic characteristics of the chemical species (e.g. binding energies; Bianchi et al. 2022) or the influence of external forces (e.g. shocks; Tercero et al. 2018; Csengeri et al. 2019; Busch et al. 2024). Studying iCOMs in external galaxies, under the assumption that they trace similar physical processes as in Galactic SF regions, may thus provide important information about the physics and the chemistry of the dense gas of extra-galactic SF regions.

Studies of iCOMs have been performed for several external galaxies, such as CH_3OH in IC 342 (Henkel et al. 1987), NGC 6946 (Eibensteiner et al. 2022), the Small Magellanic Cloud (Shimonishi et al. 2023), or PKS 1830-211 (Muller et al. 2021); CH_3CN in M82 (e.g. Mauersberger et al. 1991) and Arp 220 (Martín et al. 2011); CH_3NH_2 in PKS 1830-211 (Muller et al. 2011); HC_5N in NGC 4418 (Costagliola et al. 2015); CH_3OCH_3 in the Large Magellanic cloud (Sewiło et al. 2018; Golshan et al. 2024) or towards NGC 1068 (Qiu et al. 2018); and C_2H_5OH in NGC 253 (Martín et al. 2021), to cite a few examples. Among these galaxies, the origin of iCOMs was constrained in only a few of them, namely: CH_3OH, CH_3OCH_3, and CH_3OCHO trace hot cores in the Small and Large Magellanic Clouds (SMC and LMC, respectively; Sewiło et al. 2018; Shimonishi et al. 2023); CH_3OH traces shocks in NGC 253, NGC 1068, and M 82 (e.g. Martín et al. 2006; Humire et al. 2022; Huang et al. 2024, 2025); and CH_2NH has been found to be enhanced in the outflow of IC 860 (Gorski et al. 2023). Studies of iCOMs in extragalactic regions are thus still very limited to a few extragalactic sources, and a handful of iCOMs.

While Galactic studies offer high-resolution data on molecular cloud structure and chemistry, they are limited to relatively moderate star formation conditions. NGC 253 is a nearby (3.5 Mpc; Rekola et al. 2005), relatively edge-on (inclination of 76°; McCormick et al. 2013) galaxy hosting a starburst nucleus in its inner kpc region (Bendo et al. 2015; Leroy et al. 2015). NGC 253 provides a unique laboratory to test what we know from Galactic chemistry studies under more extreme conditions – intense radiation fields ($G_0 \sim 10^4$–10^5; Harada et al. 2022) and cosmic-ray ionisation rate ($\zeta > 10^{-14}$ s^{-1}; e.g. Holdship et al. 2022; Behrens et al. 2024), intense star formation (2 $M_\odot$ yr^{-1}; Leroy et al. 2015), and strong associated feedback processes that drive large-scale outflows (McCarthy et al. 1987). By studying iCOMs in NGC 253, we can assess whether the same assumptions used in Galactic star-forming regions hold in more extreme environments or whether additional chemical and dynamical processes dominate. This is particularly relevant for understanding the role of GMCs in starbursts and high-redshift galaxies, where similar conditions prevail but are much harder to observe in detail. So rather than merely confirming what we already know from the Milky Way, studying NGC 253 allows us to probe the universality of our chemical diagnostics and whether they remain valid in an active nuclear starburst environment.

The central molecular zone (CMZ) of NGC 253 has been surveyed by the ALMA Comprehensive High-resolution Extragalactic Molecular Inventory (ALCHEMI; Martín et al. 2021) large programme at a resolution of 1.6″ (27 pc). Previous ALCHEMI studies have revealed the chemical richness of the CMZ and how it can be used to better understand its structure and physics of the CMZ of NGC 253 (e.g. Harada et al. 2021, 2024; Holdship et al. 2022; Humire et al. 2020; Behrens et al. 2022, 2024; Huang et al. 2023; Tanaka et al. 2024; Bouvier et al. 2024; Kishikawa et al. 2025; López-Gallifa et al., in prep.). Therefore, ALCHEMI provides an ideal template to study iCOMs towards a nuclear extragalactic starburst, at a high enough angular resolution to investigate the origin of their emission for the first time. In particular, we aim to study a selection of N- and O-bearing iCOMs detected towards the CMZ of NGC 253 (Martín et al. 2021) and investigate whether spatial segregation between iCOMs at GMC scales could reflect different gas physical conditions (temperature, density), environmental conditions (e.g. heating, shocks), or evolutionary stage within the CMZ, as well as whether we can constrain their region of emission and their formation pathways. In this study, we focus on a sample of O- and N-bearing iCOMs, namely: acetaldehyde (CH_3CHO), ethanol (C_2H_5OH), formamide (NH_2CHO), methylamine (CH_3NH_2), and methanimine (CH_2NH), all previously detected in Martín et al. (2021). In addition, some of these species could be chemically linked (CH_3CHO with C_2H_5OH; e.g. Skouteris et al. 2018 and CH_3NH_2 with CH_2NH; e.g. Woon 2002; de Jesus et al. 2021; Molpeceres et al. 2024b), which will allow us to address the question of their formation pathways.

In Sect. 2, we describe the observations. We present the emission distribution and the results from the Gaussian fit of the lines in Sect. 3 and we derive the physical parameters in Sect. 4. We discuss the possible chemical pathways involved in the formation of the surveyed iCOMs, their region of emission, and the possible differences between the regions and galaxies in Sect. 5. We summarise our results in Sect. 6.

2. Observations

We used the observations from the ALCHEMI Large Programme (co-PIs.: S. Martín, N. Harada, and J. Mangum). Here, we only provide information that is relevant to the present work, while further details about the data acquisition, calibration, and imaging are given in the ALCHEMI summary paper (Martín et al. 2021). The observations were performed during Cycles 5 and 6, under the project codes 2017.1.00161.L and 2018.1.00162.S. Bands 3 through 7 were covered, with frequencies ranging between 84.2 and 373.2 GHz. The observations were centred at the position α(ICRS) = 00^{h}47^{m}33.26^s and δ(ICRS) = −25°17′17.7″. The common region imaged corresponds to a rectangular area of size 50″ × 20″ (850 × 340 pc), with a position angle of 65°, covering the CMZ of NGC 253. The data cubes have a common beam size of 1.6″ × 1.6″ (∼27 pc), a maximum recovered scale of ≳15″ (≳255 pc), and a spectral resolution of ∼10 km s^{-1}. Finally, the adopted flux calibration uncertainty is 15%, following Martín et al. (2021).

We used the continuum-subtracted FITS image cubes provided by ALCHEMI, containing the targeted species in this work. We produced velocity-integrated maps (see Sect. 3) from the processed FITS image cubes using the packages MAPPING

and CLASS from GILDAS[1]. We used these same packages to extract the spectra and perform Gaussian line fitting. The spectra were extracted from beam-sized regions before being converted to brightness temperature following Bouvier et al. (2024). For each spectrum, we fitted a zeroth-order polynomial to the line-free channels from the continuum-subtracted data cubes to retrieve the information about the spectral root mean square (rms) value.

3. Emission distribution and Gaussian line-fitting results

The CMZ of NGC 253 is a region of $300\,pc \times 100\,pc$, where ten giant molecular clouds (GMCs; named GMC 1 through GMC 10) of a size of about 30 pc in diameter have been identified in both molecular and continuum emission (Sakamoto et al. 2011; Leroy et al. 2015). At a higher angular resolution, it was found that the GMCs located in the inner 160 pc in length of the CMZ (corresponding to GMCs 3, 4, 5, and 6) can be resolved into multiple star-forming clumps called proto-super star clusters (hereafter, pSSCs; e.g. Ando et al. 2017; Leroy et al. 2018), which are compact ($\leq 1\,pc$), massive ($M \geq 10^5\,M_\odot$), and young ($\leq 3\,Myr$) clusters with ongoing star formation.

In the following, we focus our analysis in the inner part of the CMZ, which includes the regions named GMC 3 to GMC 7 (Leroy et al. 2015). This is where all the five iCOMs investigated in this work are the most intense. However, whilst the peak of the iCOMs emission coincides well with the location of GMC 6 and GMC 7, it is slightly shifted ($\lesssim 1.6''$) with respect to GMC 3 and GMC 4 (see Fig. 1a) and seems to be more consistent with the location of pSSCs. The coordinates used to extract the spectra are those of the pSSC 2 and pSSC 5 sources (see Sect. 3.2); thus, we use the name of these pSSCs for the regions that would correspond to GMC 3 and GMC 4, respectively. We note that the angular resolution of ALCHEMI does not allow us to distinguish each individual pSSC, which means that our position named pSSC 2 does in fact include pSSCs 1–3; in addition, our position labelled pSSC 5 includes pSSCs 4–7 (see Leroy et al. 2018 for the pSSCs distribution). The region GMC 6 hosts pSSC 14, but since the coordinates used to extract the spectra are centred on the coordinates of GMC 6 and not on those of pSSC 14 (which slightly differs), we kept the name GMC 6. No pSSCs have been detected towards GMC 7.

Finally, the emission of the iCOMs studied in this work is relatively faint towards GMC 5, which lies close to the kinematic centre. Moreover, this region shows particular absorption features due to the strong radio continuum emission (Meier et al. 2015; Humire et al. 2022) and would require a specific radiative transfer modelling, which is beyond the scope of this paper. We thus excluded this GMC from our analysis. As a result, in the rest of the paper, we focus on positions which we named as GMC 7, GMC 6, pSSC 2, and pSSC 5, whose coordinates are listed in Table 1. Below, we describe and compare the emission distribution of the selected species towards these four regions in Sect. 3.1 and we describe the extraction and analysis of the spectral lines in Sect. 3.2.

3.1. Emission distribution

To generate the moment maps, we looked for transitions that were isolated enough (i.e. with either no contribution from other adjacent species or with a contamination from adjacent features

that is below 3σ level) within the range of velocity on which we integrate the emission. We then integrated the emission over the full line profile, taking into account the velocity shift across the regions; hence, within the range of $[70; 380]\,km\,s^{-1}$. The transitions used to perform these moment maps are labelled in the spectra of the brightest region, GMC 6, in the figures of Appendix B on Zenodo. The corresponding spectral parameters of the transitions are shown in the same appendix.

Figure 1 shows the integrated line emission distribution of the five iCOMs, grouped in four E_u ranges, to minimize biases due to different excitation conditions. For each E_u range, we superposed the contour maps of the various species to visually show the overlap between their emission distribution. Since we have a limited sample of moment 0 maps for the five iCOMs, we could not always simultaneously compare their emission distribution at each E_u range. Panel a of Figure 1 shows the contour maps of the CH_2NH and CH_3NH_2 transitions close to $E_u = 20\,K$. Panel (b) shows the contour overlap of all species except CH_3NH_2 at $E_u = 30$–$40\,K$. Panel (c) shows the contour maps of the CH_2NH and CH_3CHO transitions at $E_u \sim 70\,K$. Finally, panel d shows the contour maps of CH_2NH and NH_2CHO around $E_u > 100\,K$.

From Figure 1, we can see a difference in the spatial emission of the iCOMs across the four regions. First, CH_3NH_2 shows more extended emission than CH_3CHO towards the part of the CMZ encompassing the regions GMC 6 to pSSC 2, as seen in Figure 1, panel a. On the other hand, the emission of CH_3CHO dominates towards GMC 7 compared to that of CH_3NH_2. For the transitions with upper energy levels around ~ 30–$40\,K$ (see Figure 1b), we can see that each GMC seems to show a different chemical composition: the CH_2NH and C_2H_5OH emission dominate GMC 7 and show the most extended emission throughout the regions. However, there is a lack of C_2H_5OH emission towards the kinematic centre (indicated by a black triangle in Figure 1) compared to CH_2NH. On the other hand, the emission of CH_3CHO and NH_2CHO is more compact around the GMCs. Both species show emission towards GMC 6 and have faint emission toward GMC 7, but whilst CH_3CHO emission covers both pSSC 5 and pSSC 2, NH_2CHO lacks emission towards pSSC 2. At $E_u \sim 70\,K$ (see Figure 1c), both CH_2NH and CH_3CHO show emission towards GMC 6 with CH_2NH showing a slightly more spatially extended emission compared to CH_3CHO. On the other hand, only CH_2NH emits towards pSSC 5 and the two species are fainter towards pSSC 2 and GMC 7. For $E_u > 100\,K$ (see Figure 1d), we see that both CH_2NH and NH_2CHO emit towards GMC 6 and pSSC 2 but CH_2NH shows a more extended emission. CH_2NH only emits towards pSSC 5 and both species are absent at GMC 7. Interestingly, whilst NH_2CHO showed fainter emission for $E_u \sim 30$–$40\,K$ towards pSSC 2, it shows stronger emission for $E_u > 100\,K$. Whilst the emission of the iCOMs seems to show a spatial disparity within the inner GMCs of NGC 253, we should keep in mind that fainter emission could be due to either a true lower abundance or a sensitivity bias if the transition is not very intense (band 5 observations were less sensitive compared to the rest of the data; see Martín et al. 2021). Hence, the investigation of whether there is a disparity among the species across the region comes after we have derived the physical parameters (Sect. 4).

Finally, we can see an evolution in the emission morphology compared to E_u: Looking at CH_3CHO and CH_2NH for which we imaged transitions from 19 K to 70.5 K and from $\sim 40\,K$ to $\sim 123\,K$, respectively, we see the emission being more compact with increasing E_u. This shows that transitions with different E_u may be excited under different conditions and it is important
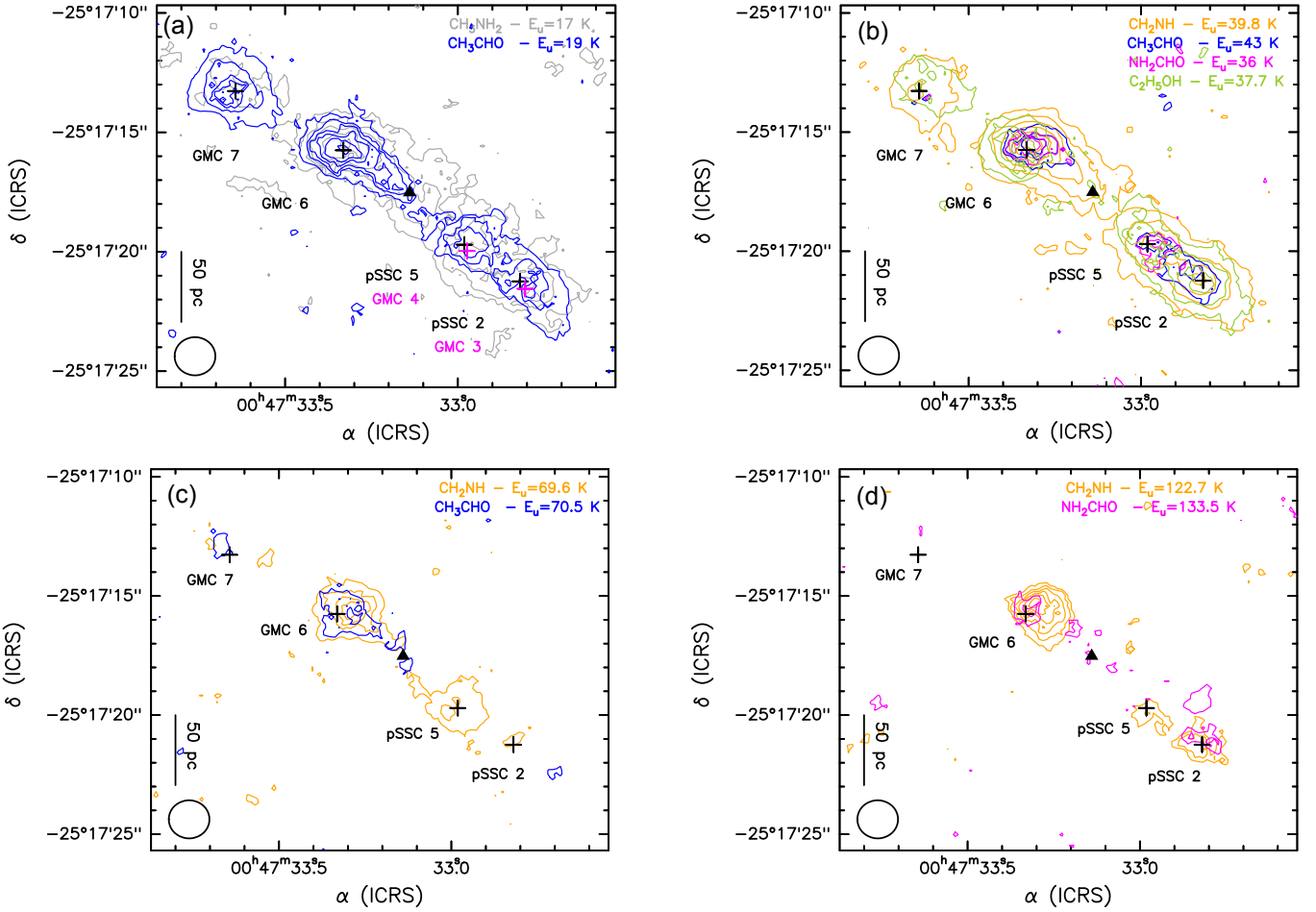
Fig. 1. Overlap of contours corresponding to the velocity integrated species emission, ordered by their upper energy level, E_u. A spatial scale of 50 pc corresponds to $\sim 3''$. The kinematic centre ($\alpha_{ICRS} = 00^h47^m33.14^s$ and $\delta_{ICRS} = -25°17'17.52''$; Müller-Sánchez et al. 2010) is labelled by a filled black triangle. The black crosses mark the positions analysed in this work and correspond to GMC 7, GMC 6, pSSC 5 and pSSC 2. For reference, the position of GMC 3 and GMC 4 (Leroy et al. 2015) are indicated by magenta crosses in the panel a. The beam size if depicted in the lower left corner of each box. Contours of CH_3NH_2, CH_3CHO, CH_2NH, NH_2CHO, and C_2H_5OH are in grey, blue, orange, magenta, and green, respectively. *a)* Contour overlap of CH_3NH_2 ($3_{-1,1}-2_{0,0}$; $E_u = 17$ K) and CH_3CHO ($1_{1,5}-1_{0,5}$ (E+A); $E_u = 19$ K). Contours start at 3σ with steps of 3σ with $1\sigma = 42$ and 25 mJy beam^{-1} km s^{-1}, respectively. *b)* Contour overlap of CH_2NH ($4_{1,3}-3_{1,2}$; $E_u = 39.8$ K) with $1\sigma = 78$ mJy beam^{-1} km s^{-1}, CH_3CHO ($9_{2,9}-8_{1,8}$ (E+A); $E_u = 43$ K) with $1\sigma = 55$ mJy beam^{-1} km s^{-1}, NH_2CHO ($8_{0,8}-7_{0,7}$; $E_u = 36$ K) with $1\sigma = 58$ mJy beam^{-1} km s^{-1}, and t-C_2H_5OH ($6_4 - 5_3$; $E_u = 37.7$ K) with $1\sigma = 64$ mJy beam^{-1} km s^{-1}. Contours start at 3σ with steps of 3σ for CH_3CHO and t-C_2H_5OH, 8σ for CH_2NH, and 2σ for NH_2CHO. *c)* Contours overlap of CH_2NH ($6_{1,6}-5_{1,5}$; $E_u = 69.6$ K) with $1\sigma = 42$ mJy beam^{-1} km s^{-1} and CH_3CHO ($11_{2,9}-10_{2,8}$ (E+A); $E_u = 70.5$ K) $1\sigma = 25$ mJy beam^{-1} km s^{-1}. Contours start at 3σ with steps of 5σ and 3σ for CH_2NH and CH_3CHO, respectively. *d)* Contour overlap of CH_2NH ($8_{1,7}-8_{0,8}$; $E_u = 122.7$ K), with $1\sigma = 61$ mJy beam^{-1} km s^{-1} and NH_2CHO ($15_{2,14}-14_{2,13}$; $E_u = 133.5$ K) $1\sigma = 78$ mJy beam^{-1} km s^{-1}. Contours start at 3σ with steps of 2σ.

Table 1. Selected regions and coordinates.

Region	RA (ICRS) (00^h47^m)	Dec (ICRS) ($-25°$:17')
GMC 7	$33^s.6432$	$13''.272$
GMC 6	$33^s.3312$	$15''.756$
pSSC 5	$32^s.9811$	$19''.710$
pSSC 2	$32^s.8199$	$21''.240$

Notes. GMC stands for giant molecular Cloud and pSSC stands for proto-super star cluster.

to compare spatial extent of species which have similar upper level energies. All the velocity-integrated maps obtained for each species are shown in Figures A.1–A.5.

3.2. Spectra and line parameters

We extracted the spectra towards GMC 7, GMC 6, pSSC 5, and pSSC 2 from regions of a beam-size ($1.6'' \times 1.6''$) and centred on the coordinates given in Table 1. We then centred each spectrum at the local standard of rest velocity (LSRK) corresponding to the rest frequency of each transition used in this work before performing a Gaussian line fitting to the detected transitions. A threshold of 3σ on the intensity peak was set to consider a line to be detected. Transitions that had been contaminated by more than 15% by a transition from another species (i.e. contributing to 15% or more of the total integrated intensity of our desired transition) or that were too blended to perform a multiple Gaussian fit were not taken into account. To assess whether a line is contaminated, we used the existing line identification of ALCHEMI 7 m and 12 m data (Martín et al. 2021 and priv. comm.) and performed an additional inspection using WEEDS (Maret et al. 2011). This is an extension of CLASS

that uses both the Jet Propulsion Laboratory (JPL; Pickett et al. 1998) and the Cologne Database for Molecular Spectroscopy (CDMS; e.g. Müller et al. 2005; Endres et al. 2016) databases. However, in the case of CH_3CHO, the E- and A- states are often completely blended together and the spectral resolution of $10\,km\,s^{-1}$ is insufficient to disentangle the two states. Similarly, for NH_2CHO and CH_3NH_2, there are two transitions with similar spectroscopic parameters are completely blended together. In these cases, we still kept these transitions and performed a single line Gaussian fit. We explain how we used these transitions for the analysis in Sect. 4.1. We present the list of all of the transitions per species and per region used in this work, as well as their spectroscopic parameters, in Appendix B on Zenodo. We detected only the form anti of C_2H_5OH among the different rotamers, but this is not surprising as the form anti is the most stable rotamer (Pearson et al. 2008; Bianchi et al. 2019); thus, C_2H_5OH refers to this form only.

From the Gaussian line fitting procedure, we extracted the integrated intensities ($\int T_B.dV$) in $K\,km\,s^{-1}$, the line widths (FWHM), and the peak velocity (V_{peak}), both in $km\,s^{-1}$. The extracted spectra, the best Gaussian fits and a summary of the Gaussian line-fitting results and rms for each transition and region are available in Appendix B on Zenodo.

4. Derivation of the physical parameters

4.1. Methodology

For each species and each of the four selected regions, we detected enough transitions (>7 for most species and regions) with a broad enough range of E_u covered to derive the column densities and rotational temperatures using the rotational diagram (RD) method (Goldsmith & Langer 1999). This method assumes local thermodynamic equilibrium (LTE) and optically thin emission. These assumptions are revisited later in this work based on the case of CH_2NH (see Sect. 4.3). We also assumed the Rayleigh-Jeans approximation holds. We included a calibration error of 15% (see Sect. 2) and the spectral rms in the integrated flux uncertainties. The best fit was calculated by minimizing the reduced chi-square, χ_r^2.

As a first approximation, we set the beam-filling factor[2] to 1/2, assuming that our emission comes from the GMC scales (hence from a region of the size of the beam or 1.6″). However, in some regions and for some species, we saw a clear deviation in the rotational diagram for the higher E_u transitions. This behaviour can be either due to the presence of multiple gas components with different physical conditions or to non-LTE (NLTE) or opacity effects (Goldsmith & Langer 1999). We favoured the first option, namely, the presence of multiple gas components. Our choice is supported by the fact that higher upper-energy level transitions showed often a different FWHM or V_{peak} compared to the lower upper-energy transitions (see discussion in Sect. 4.2 below) and the difference in the emission distribution of the species depending on the excitation conditions (see Sect. 3.1). For these cases, we assumed that the first component, traced by the lower upper-level energy transitions, arises from the GMCs; whilst the second component, traced by the higher upper-level energy transitions, arises from the pSSCs. For the latter component, we calculated the beam-filling factor using a size for the pSSC clusters of 0.12″ (corresponding to ~2 pc), estimated by Leroy et al. (2018). This assumption is supported

by the fact that the emission is more compact with increasing E_u, which sometimes goes unresolved by the ALCHEMI beam (See Figure 1).

Finally, as mentioned in Sect. 3.2, most of the E- and A-states of CH_3CHO and some transitions for NH_2CHO, CH_3NH_2 and C_2H_5OH are too blended to perform a multiple Gaussian fit. As the blended transitions have the same spectroscopic parameters (E_u, A_{ij}, g_u), thus, we assumed that each transition accounts for 50% of the total line integrated intensity. Furthermore, for CH_3CHO, we assumed a CH_3CHO-E/CH_3CHO-A ratio of 1, since the kinetic temperature is higher than the energy difference of ~0.1 K between the levels of the different symmetry states (Matthews et al. 1985). Therefore, we included each pair of blended transitions in the RDs by attributing 50% of the total integrated intensity, given in Appendix B on Zenodo, to each individual transition.

4.2. Rotational diagrams

In Figure 2, we show as an example the rotational diagrams obtained for each species towards GMC 6, which is the region showing the most intense emission (see Sect. 3.1). The RDs at other positions are available on Appendix C on Zenodo. In the case of GMC 6, two temperature components were needed for CH_3NH_2, NH_2CHO, and CH_3CHO. Two temperature components were also needed for pSSC 2 (CH_3NH_2 and NH_2CHO) and for pSSC 5 (CH_3NH_2 and CH_3CHO). For CH_3NH_2 and CH_3CHO, the deviation occurs near $E_u \sim 40\,K$ and it is closer to 60 K for NH_2CHO. When two temperature components are present in the RDs, we made the assumption that they are not arising from the same spatial component. The low E_u transitions being more spatially extended compared to the higher E_u transitions (see Sect. 3.1), we assumed that whilst the former mainly arises from GMC scales, the latter arises from more compact scales, such as the pSSC scales (i.e. the structures identified next within the GMCs). As a caveat, this implies that the contribution from the warm compact component to the cold extended one is negligible.

For the species showing two temperature components, we looked at the Gaussian fit results to check for any shift in the mean FWHM or V_{peak} as a function of the upper-level energy. In the following, we discuss first about the Gaussian fit results in the context of the two temperature components (Sect. 4.2.1) before discussing the results from the RDs (Sect. 4.2.2).

4.2.1. Gaussian fits and temperature components

To check whether the presence of the two temperature components seen in the RDs for CH_3CHO, CH_3NH_2, and NH_2CHO can be identified through a shift in the mean FWHM or V_{peak} as a function of the upper-level energy, we used only relatively isolated transitions, where a single Gaussian fit was performed to get the most reliable measurement for FWHM and V_{peak}. In the case of auto-blended transitions, we kept only those for which the two lines are separated enough to perform two separate Gaussian fits. Figure 3 shows the FWHM and V_{peak} as a function of E_u towards GMC 6, pSSC 5, and pSSC 2, where a second gas component has been fitted in the RDs. The uncertainties were derived by adding in quadrature the errors from the Gaussian fits with the spectral resolution of $10\,km\,s^{-1}$. The mean FWHM and V_{peak} for each component are summarised in Table B.2 on Zenodo. We discuss the individual species below:

---

[2] We used the formula $\eta_{ff} = \left(\theta_S^2/(\theta_S^2 + \theta_B^2)\right)$ with θ_S as the source size and θ_B as the beam size of the ALCHEMI observations.
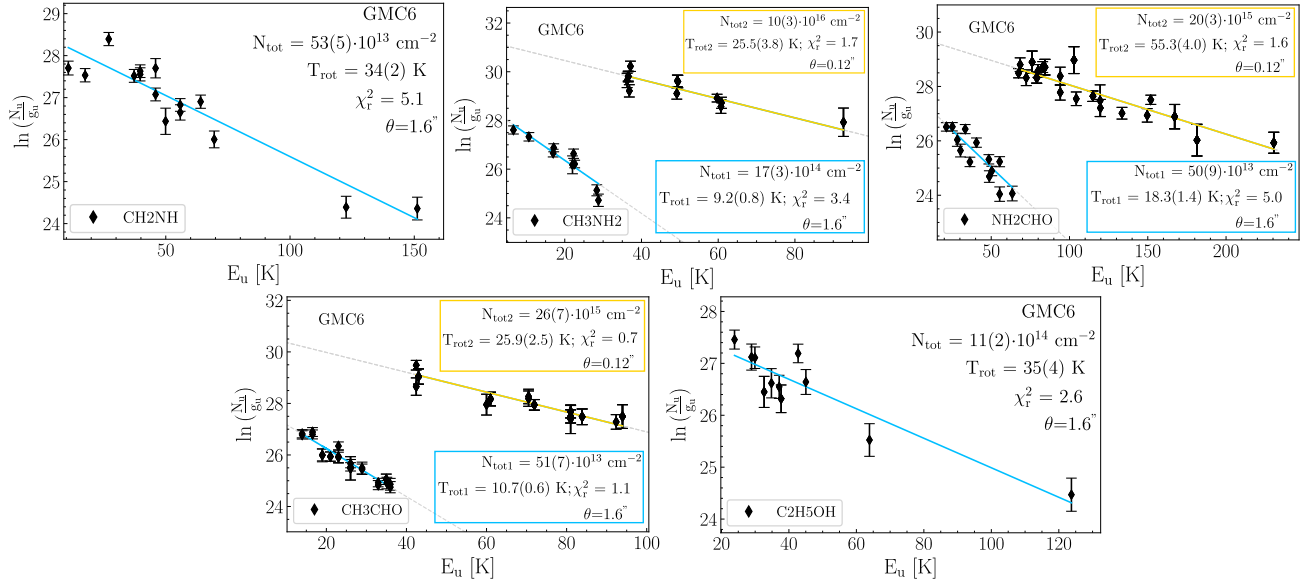
Fig. 2. Rotational diagrams of each species towards GMC 6. Parameters E_u, N_u, and g_u are the level energy (with respect to the ground state), column density, and degeneracy of the upper level, respectively. The error bars on $\ln(N_u/g_u)$ include a calibration error of 15% (see Sect. 2). The blue (and orange if a second component is fitted) solid lines represent the best fits and the dashed grey lines are the extrapolations of the fit for the full range of E_u covered. The source size assumed is indicated for each component (see Sect. 4.1).

CH$_3$CHO (Figure 3, top panels): We see a clear difference in the mean V_{peak} for GMC 6, where we see an increase in the V_{peak} with increasing E_u. However, we cannot see this shift toward pSSC 5, where a second temperature component has also been fit in the RD (see Appendix C on Zenodo), due to the lack of reliable Gaussian fit measurements.

CH$_3$NH$_2$ (Figure 3, middle panels): A slight decrease in the line widths with increasing E_u is seen towards GMC 6 and pSSC 5, although it is quite marginal. No variation in the FWHM is seen towards pSSC 2 and no difference in the V_{peak} is seen towards any of the regions in CH$_3$NH$_2$. Thus, we find no strong indication of two different components for CH$_3$NH$_2$ and the deviation in the RD could be due to NLTE effects (Goldsmith & Langer 1999).

NH$_2$CHO (Figure 3, bottom panels): An increase in V_{peak} is relatively clear with increasing E_u towards the two regions where two components were fitted (i.e. GMC 6 and pSSC 2). For pSSC 2, we also observe a decrease in the FWHM simultaneously with an increasing E_u, and this can be seen more moderately towards GMC 6. Interestingly, the shift in V_{peak} and in FWHM seems to occur closer to 40, compared to what is seen in the RDs, which could indicate that the majority of the NH$_2$CHO emission could be associated with the second higher temperature component.

In conclusion, with the current spectral resolution as a main contributor to the uncertainties, the presence of two components is only clear for NH$_2$CHO, whilst it is not clear for CH$_3$CHO and CH$_3$NH$_2$. In addition, we should note that optically thick lines can induce larger line widths. Higher spectral and angular resolution observations are needed to identify possible different gas components more clearly.

4.2.2. Results from the rotational diagrams

Figure 4 shows an overview of the derived T_{rot} and N_{tot} for each species and region listed in Table C.1 on Zenodo. Due to the fact

that we observe deviations from the fits in the RDs, it is clear that the derived T_{rot} values are not representative of the true gas temperature. For the rotational temperatures (top panel of Figure 4), we do notice some differences between the regions. In particular, GMC 7 shows only a cold ($T_{rot} \leq 20$ K) component compared to the other regions. On the other hand, the other regions have two components, a cold ($T_{rot} \leq 20$ K) and a warmer component ($T_{rot} \sim 30-80$ K). Finally, none of the regions shows a hot ($T_{rot} > 100$ K) component, which would have been expected if the iCOMs were thought to be emitted from a hot-core-like ($T > 100$ K; see e.g. Kurtz et al. 2000) region. On the other hand, this result is similar to the Milky Way's Galactic Centre (GC), where widespread emission (a few tens to hundreds of parsecs) from iCOMs has been measured (e.g. Requena-Torres et al. 2006; Li et al. 2017, 2020). There, low rotational temperatures ($T_{rot} \leq 20$ K; e.g. Requena-Torres et al. 2006; Zeng et al. 2018; Rivilla et al. 2022b) were also derived, indicating that the GC iCOM emission is sub-thermally excited. The extended iCOM emission toward the GC is not associated with hot cores and can be explained by widespread recurrent low-velocity shocks (Requena-Torres et al. 2006; Zeng et al. 2020).

For the column densities (bottom panel of Figure 4), we describe the behaviour separating the emission from the cold component (derived with $\theta_s = 1.6''$; i.e. GMC scale) and the warm component (derived with $\theta_s = 0.12''$, i.e. pSSC scale) transitions, as given below. Only one temperature component was fitted for all species towards GMC 7, CH$_2$NH and C$_2$H$_5$OH towards all regions, NH$_2$CHO towards pSSC5, and CH$_3$CHO towards pSSC2. In these cases, since we did not have knowledge of the region of emission of these species, we calculated the column densities for the two emission sizes, namely: for the GMC scale ($\theta_s = 1.6''$) and pSSC scale ($\theta_s = 0.12''$).

GMC-scales: C$_2$H$_5$OH and CH$_3$CHO show relatively constant column densities throughout the regions. On the other hand, NH$_2$CHO, CH$_3$NH$_2$, and CH$_2$NH show a decrease in N_{tot} towards GMC 7 and the column density of CH$_3$NH$_2$ increases
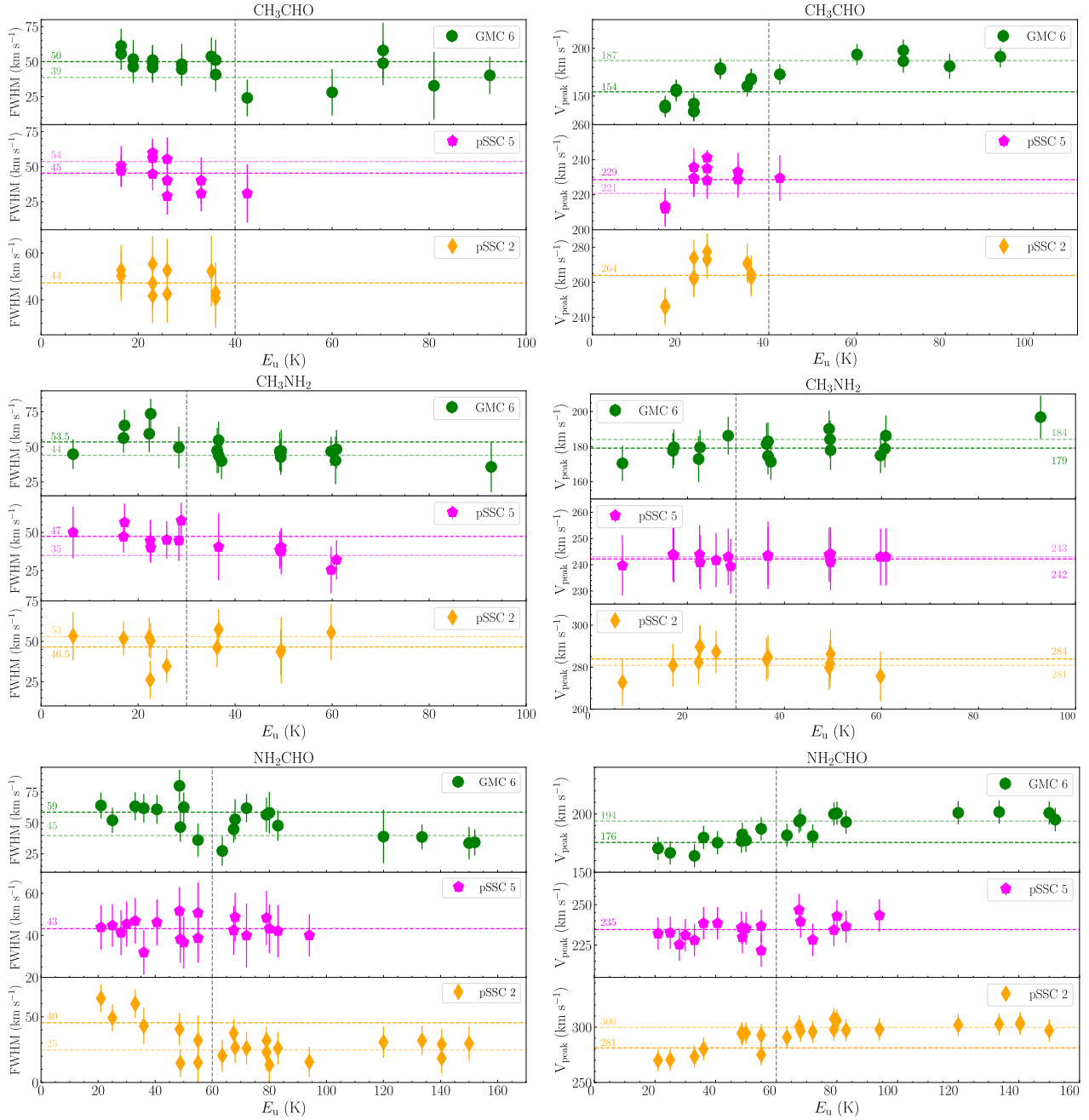
Fig. 3. Line widths (FWHM; left-hand side) and peak velocities (V_{peak}; right-hand side) as a function of upper level energies (E_u) for CH_3OH (top panels), CH_3NH_2 (middle panels), and NH_2CHO (bottom panels) and for GMC 6 (filled green circles), pSSC 5 (filled magenta pentagons), and pSSC 2 (filled orange diamonds). The vertical dashed grey lines indicate where the deviation in the RDs occurs, i.e. ~40 K, 30 K, and 60 K for CH_3CHO, CH_3NH_2, and NH_2CHO, respectively. Only the most clear Gaussian fits have been used (see text). If a second component has been identified in the RDs, it is shown in lighter color. Mean FWHM and V_{peak} are indicated on the plots by horizontal dashed lines accompanied with their corresponding values.

towards GMC 6. Overall, C_2H_5OH and CH_3NH_2 show the highest column densities, except towards GMC 7 where the column density of CH_3NH_2 decreases.

pSSC-scales: For C_2H_5OH and CH_2NH, the trend in column density is the same as at GMC-scales since the two species have only one component. In the case of CH_3NH_2, its column density is constant across the regions except towards GMC 7, where it decreases. In the cases of NH_2CHO and CH_3CHO, if we consider only the second components (high E_u) towards GMC 6 and pSSC 5 for CH_3CHO and pSSC 2 for NH_2CHO, then the col-

umn density of both species is the highest towards GMC 6. If we consider that in the other regions where only one component is detected (low E_u transitions), then the column density of CH_3CHO is the lowest towards pSSC 5 and that of NH_2CHO is the lowest towards GMC 7 and pSSC 2.

We note that since the four regions do not have the same H_2 column densities, the abundance trends could be different than the column density trends. However, an abundance study is beyond the scope of this paper. We simply stress here that there are variations of the relative column densities between the species across the regions, indicating possible chemical
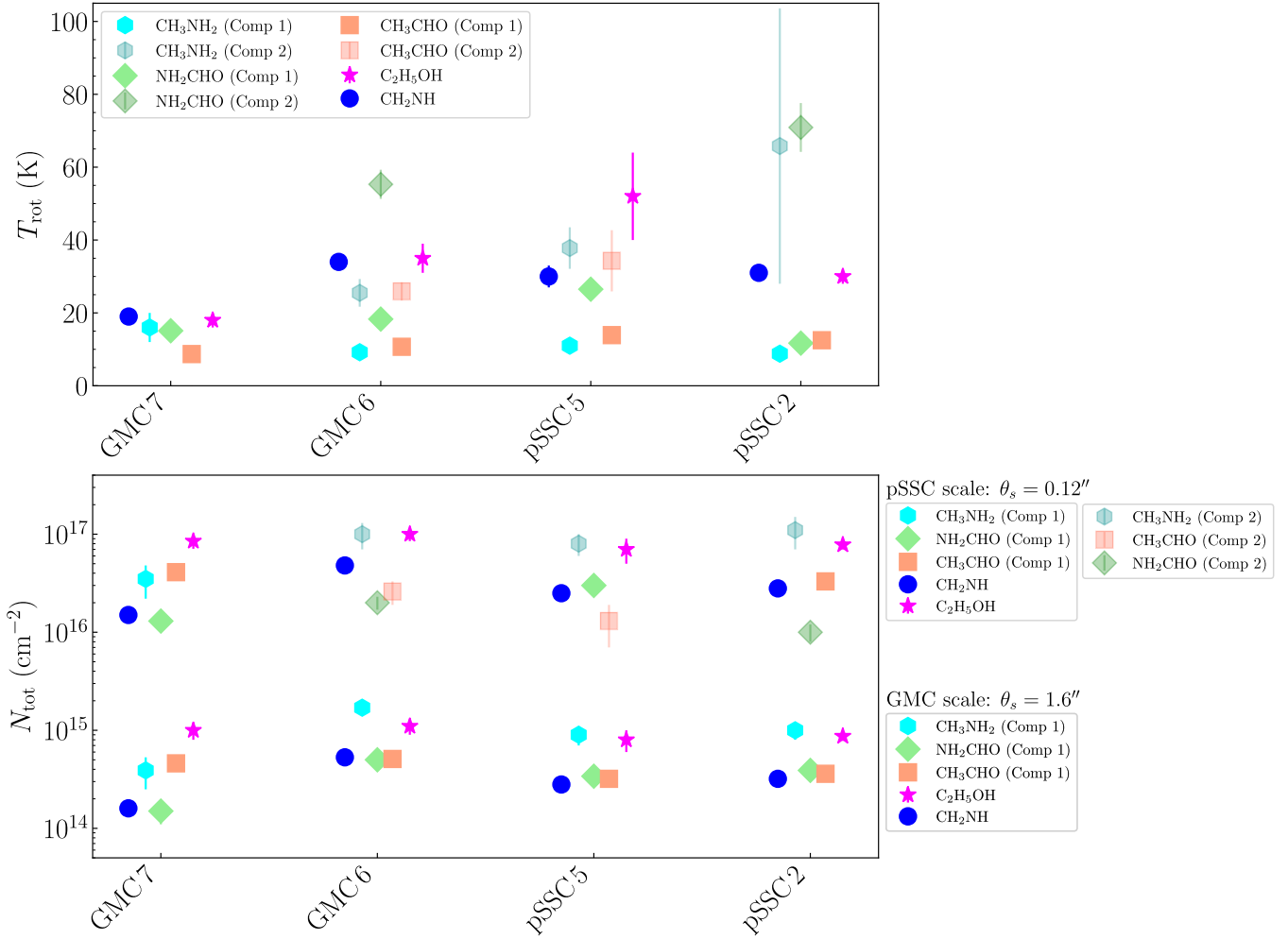
Fig. 4. Derived rotational temperature (T_{rot}; top) and total column density (N_{tot}; bottom) for each species and region. The order of the regions follows the layout of the GMCs/SSCs of the CMZ from north-east to south-west as shown in Figure 1. Top: when two gas components were fitted in the RDs, the T_{rot} of the two components are indicated. Bottom: column densities derived for GMC scales ($\theta_s = 1.6''$; bottom part) and pSSC scales ($\theta_s = 0.12''$; top part). For the species (CH$_2$NH and C$_2$H$_5$OH) and region (GMC 7), where only one gas component was fitted, we calculated the column densities for the two scales. For the other regions and species, we attributed the first component to an emission coming from GMC scales and the second component to an emission coming from pSSC scales. In the cases of NH$_2$CHO and CH$_3$CHO, only one component was fitted for pSSC 2 and pSSC 5, respectively.

differences, for instance, towards GMC 7, where the relative amount between O-bearing and N-bearing iCOMs changes compared to the other regions. We discuss chemical variations in more details in Sect. 5.3.

4.3. NLTE analysis: CH$_2$NH

CH$_2$NH is the only species from this work for which collisional excitation rates are available. Therefore, we can perform a NLTE analysis to constrain more accurately the gas physical parameters traced by CH$_2$NH toward the CMZ of NGC 253.

We performed this analysis using the large velocity gradient (LVG) code `grelvg` (Ceccarelli et al. 2003). We used the CH$_2$NH–H$_2$ collisional rates from Xue et al. (2024) available in the Excitation of Molecules and Atoms for Astrophysics (EMAA) database[3]. The rates were calculated for a temperature in the range 10–150 K and for the transitions up to $E_u = 143$ K. Therefore, the maximum temperature tested is limited by the available rate coefficients and the CH$_2$NH transition at

312.336 GHz with $E_u = 151.3$ K, which we detected in this work, was excluded from the analysis. For each region we ran a grid of models (~10 000), varying the column density, the gas density, and temperature within 10^{13}–10^{18} cm^{-2}, 10^4–10^8 cm^{-3}, and 10–150 K, respectively. The column densities and gas densities were both sampled in logarithmic scale and the gas temperature was sampled in linear scale. We left the source size as a free parameter. Then, for the geometry, we chose a uniform sphere (Osterbrock 1974) as the most physically realistic choice. The ortho-to-para ratio of H$_2$ was set to the statistical value of 3. Finally, the average line widths of CH$_2$NH chosen is 50 km s^{-1}, which is the average line width across the regions (see Table B.2 on Zenodo). We also included a 15% calibration uncertainty in the integrated intensity (see Sect. 2).

From the RD analysis, there is no clear indication of a multiple temperature components for CH$_2$NH (see e.g. Figure 2). We thus first included all the lines in the LVG code. However, this resulted in a bad fit ($\chi_r^2 > 5$) for GMC 6, pSSC 5, and pSSC 2. In these regions, the two transitions of CH$_2$NH at 225.554 and 172.267 GHz are not well fit with the other transitions. These lines have the lowest E_u (<20 K) and could thus be coming from
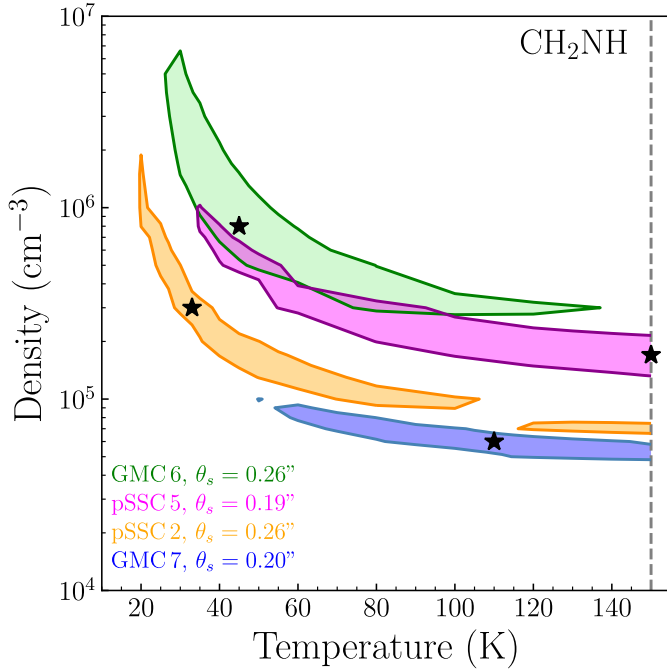
---

[3]   https://emaa.osug.fr/

Fig. 5. Volume density and kinetic temperature contour plots showing the results from the LVG analysis for CH_2NH towards GMC 7 (blue), GMC 6 (green), pSSC 5 (magenta), and pSSC 2 (orange). The contours show the 1σ solutions obtained for the minimum χ_r^2 value in the column density parameter. The best fits are marked by black stars, while the best fit for the emission size (θ_s) are indicated in the bottom-left corner of the figure. The vertical grey line indicates the maximum temperature at which the rates are calculated.

a cooler or more extended component compared to what the other transitions ($E_u = 27-151$ K) trace. Since we cannot perform the LVG analysis with only two lines, we cannot constrain the physical parameter of this potentially cooler component. We thus ran the LVG with the rest of the lines ($E_u \geq 27$ K).

Figure 5 shows the results of the LVG analysis for each of the four regions. The best fit for the CH_2NH column densities is similar towards the four regions with values in the range $(1.5-2) \times 10^{16}$ cm^{-2}. The kinetic temperatures are not always well constrained and are limited by the maximum temperature available from the collisional rates (150 K). We thus have an overall lower limit of $T_{kin} \geq (20-50)$ K across the different regions. For the derived gas densities, they lie mostly between $n(H_2) = (10^5-10^6)$ cm^{-3} except for GMC 7, where $n(H_2) \leq 10^5$ cm^{-3}. In all the regions, several lines were found to be optically thick with $\tau > 1$ (see Table 2). Finally, the best fit for the emission size is in the range $0.19'' - 0.26''$ corresponding to a linear scale of ~3–4 pc in diameter. The best-fit solutions and ranges obtained for each source are reported in Table 2. The 1σ confidence levels constrained correspond to a 68% confidence range.

We corrected the rotational diagram for the optical depth and source size for all the regions using the population diagram method (Goldsmith & Langer 1999), taking the output values of the LVG analysis for these parameters to investigate whether the optical depth effects are dominant. For consistency, we removed the transitions that were left out from the LVG analysis (see above). The corrected RDs are shown in the Appendix C on Zenodo. We still found some deviation from a straight line in the corrected RDs, with rotational temperatures below the minimum gas temperature predicted by the LVG analysis. There-

fore, we find that CH_2NH is also affected by NLTE effects. This result is consistent with that of Faure et al. (2018), who found that NLTE effects can be expected in the density range of $n_{H_2} = 10^3-10^7$ cm^{-3} for this species. We do note, however, that in the discussion below, we use the column densities derived with the RDs for CH_2NH, since the goal of performing population diagrams was only to evaluate the contribution of NLTE effects.

5. Discussion

As mentioned in the introduction, investigating iCOMs in more extreme star formation conditions than those found in our own Galaxy allows us to probe the universality (or otherwise) of our chemical diagnostics and whether they remain valid in extragalactic environments. Below, we qualitatively discuss whether the known proposed formation pathways for iCOMs could also be valid in NGC 253 and whether the iCOMs in this study can be chemically linked (Sect. 5.1). We then discuss their possible region of emission and the physical processes they might be tracing (Sect. 5.2). Finally, we focus on the small chemical differences within the regions (Sect. 5.3). Figure 7 shows a schematic summarising our main hypotheses and scenarios concerning iCOMs towards the CMZ of NGC 253, focussing in particular on the discussion from Sects. 5.1 and 5.2.

5.1. Chemical link and formation pathways for iCOMs

Understanding which chemical pathways to the formation of a specific species are dominant within an environment is not straightforward. From observations, a method that is regularly used is to look at the abundance correlations between two species suspected to be chemically linked or to have a similar precursor (e.g. Yamamoto 2017; Coletta et al. 2020; Li et al. 2024). However, it is worth noting that a correlation between two species does not always imply a direct chemical link. It may also indicate that they went through similar physical processes of formation across different environments (e.g. Quénard et al. 2018; Belloche et al. 2020).

Figure 6 shows the relation between the column densities of the iCOMs, at both GMC scales (corresponding to a source size of 1.6'') or pSSC scales (corresponding to a source size of 0.12''). We list below several trends from Figure 6 that will be discussed below. We refer to CH_3CHO and C_2H_5OH as O-bearing iCOMs, and then CH_2NH and CH_3NH_2 as N-bearing iCOMs, while NH_2CHO lies in between the two categories.

- At GMC scales, O-bearing species are well correlated over the four regions and present a constant ratio $[C_2H_5OH/CH_3CHO]$ of 3 (panel a). The correlation disappears at pSSC scales (panel f).
- At both GMC- and pSSC scales, there is an enhancement in O-bearing species compared to N-bearing species (including NH_2CHO) towards GMC 7 (panels b, c, h, and k).
- At GMC scales, CH_3NH_2 and NH_2CHO are relatively well correlated over the four regions and present a constant ratio $[CH_3NH_2/NH_2CHO]$ of ~3 (panel d). At pSSC scales, the ratio increases towards GMC 7 and pSSC 2 (panel i).
- The ratio $[CH_3CHO/NH_2CHO]$ varies greatly from GMC scales (panel b) to pSSC scales (panel g).
- The abundance ratio between CH_3NH_2 and CH_2NH (panels e, j) is close to 3 at both scales, but slightly lower for GMC 6 at pSSC scales.

Table 2. Best fit results and 1σ confidence level range from the NLTE LVG analysis of CH$_2$NH.

Parameters	GMC 7		GMC 6		pSSC 5		pSSC 2	
	Best fit	Range	Best fit	Range	Best fit	Range	Best fit	Range
N_{CH_2NH} ($\times 10^{16}$ cm^{-2})	1.5	0.7–4.5	1.5	0.7–4	2	0.2–5	2	0.2–5
$n(H_2)$ ($\times 10^5$ cm^{-3})	0.6	0.5–1	8	3–60	1.7	1–10	3	0.7–20
T_{kin} (K)	110	≥ 45	45	25–130	150	≥ 30	33	20–100 ; ≥ 120
Source size ($''$)	0.20	0.15–0.24	0.26	0.16–0.34	0.19	0.17–0.60	0.26	0.22–0.60
τ range	0.6–3.4		0.04–1.3		0.03–2.4		0.01–2.3	
χ_r^2	0.3		1.3		1.4		1.7	
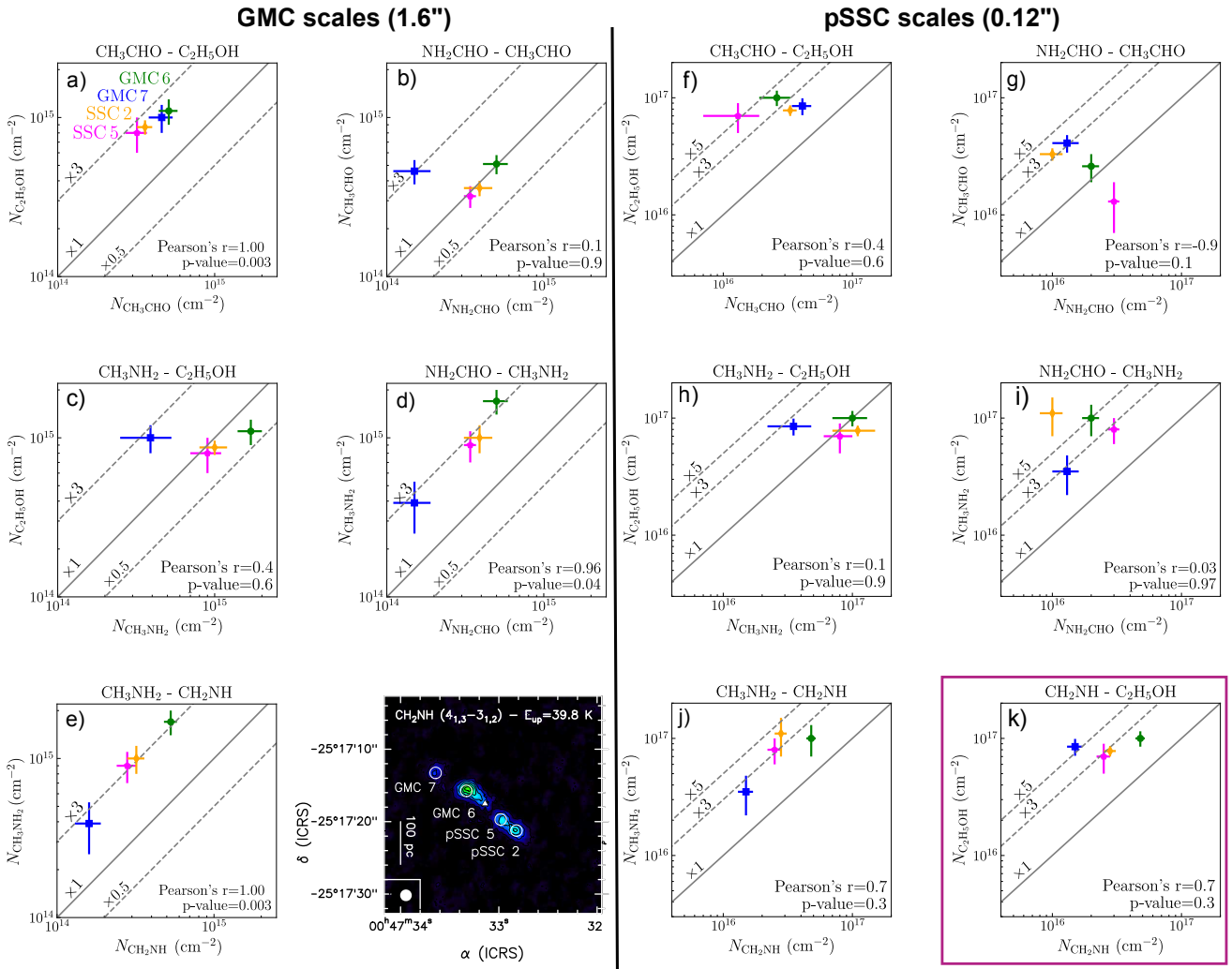
Fig. 6. Relation between the column densities of the iCOMs derived from the rotational diagrams at GMC scales ($\theta = 1.6''$; left-hand side of the figure) and at pSSC scales ($\theta = 0.12''$; right-hand side of the figure), for each region (GMC 7: blue; GMC 6: green; pSSC 5: magenta; pSSC 2: orange). Pearson's coefficient and p-values are indicated in the bottom right part of each plot. Dashed and full grey lines indicate abundance ratio factors. Panel k is highlighted as the correlation between CH$_2$NH and C$_2$H$_5$OH is the same at both GMC-scale and pSSC-scale. For reference for the location of each region, we added a map of the CH$_2$NH ($4_{1,3}-3_{1,2}$) transition in the bottom-left part of the figure.

In the following sub-sections, we look for correlations between the derived column densities of a few pairs of iCOMs, which are thought to share chemical roots. We first recall the known formation pathways of the different species before discussing whether a certain formation pathway is most probable for the CMZ of NGC 253, as well as whether a chemical link between the pairs of species discussed is possible. A summary of plausible formation pathways for each iCOM is shown in Figure 7.

5.1.1. CH$_3$CHO and C$_2$H$_5$OH

The formation pathways of CH$_3$CHO are debated. Both gas-phase and grain-surface reactions are proposed. Among the viable gas-phase formation pathways, CH$_3$CHO could be formed either from the radical C$_2$H$_5$ previously formed on the grain and ejected in the gas phase (e.g. Charnley 2004; Vasyunin & Herbst 2013; Barger & Garrod 2020; Codella et al.
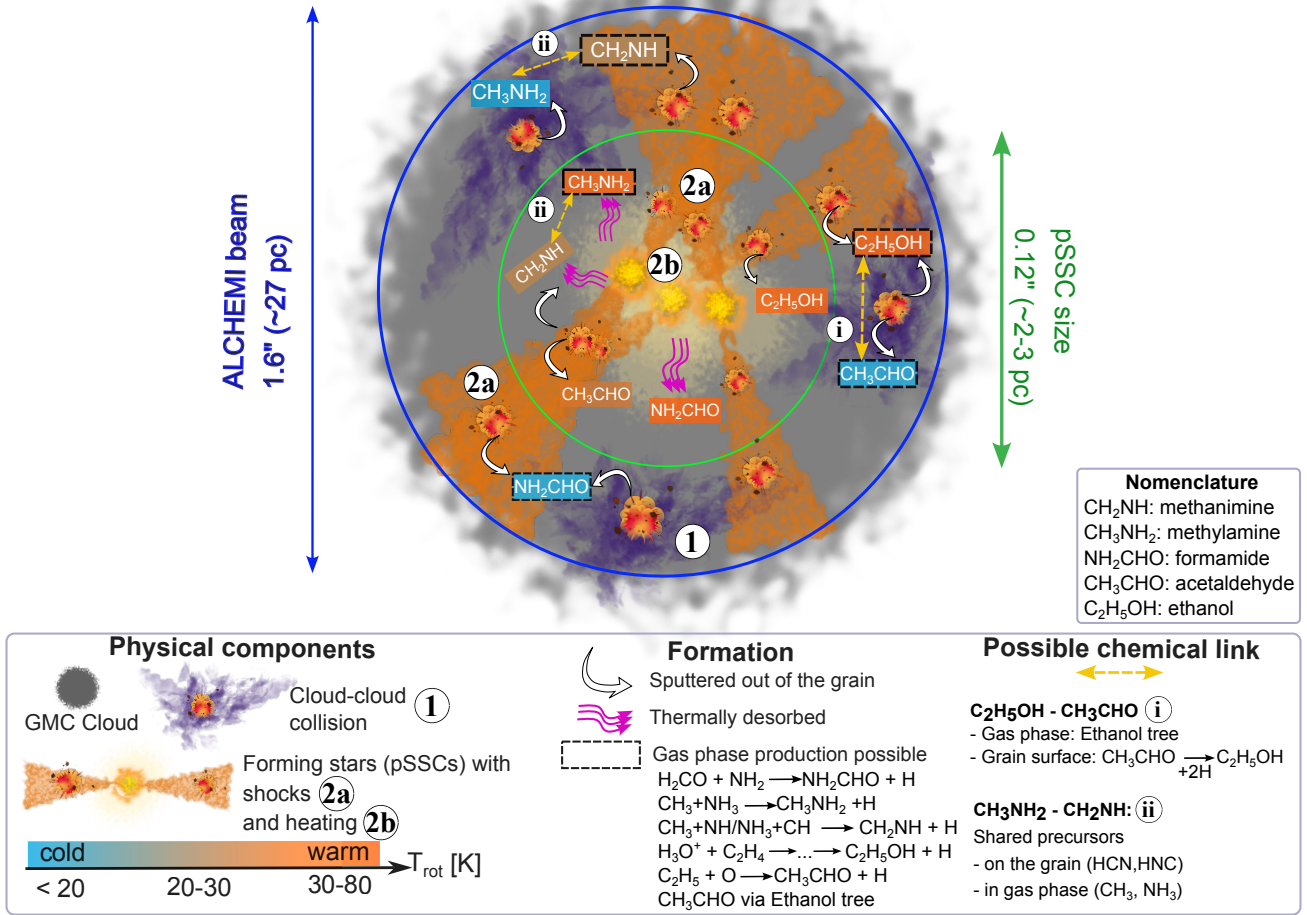
iCOMs towards the CMZ of NGC 253

Fig. 7. Schematic (not to scale) of summarising the possible formation pathways and chemical links between the iCOMs (Sect. 5.1) and their emission origins (Sect. 5.2) within a GMC. The temperatures reported are averaged over the region but there can be variation from one region to another. We assume the size of a GMC is comparable or larger than the size of the ALCHEMI beam of 1.6″ (or ~27 pc). Formation and chemical links: Sputtering from the ice grain mantle and gas phase formation pathways are both possible to explain the iCOM emission at GMC scales, whilst at SSC scales, the dust temperature can be high enough to allow thermal desorption. CH_3CHO and C_2H_5OH can also be chemically linked (i) both on the grain (with CH_3CHO as the precursor of C_2H_5OH) or via the Ethanol tree in the gas phase (with C_2H_5OH as a precursor for CH_3CHO). CH_3NH_2 and CH_2NH could be chemically linked (ii) by sharing similar precursors, both on the grain or in the gas phase (if the gas temperature is higher than 100 K; e.g. Halfen et al. 2013). Origin: At the scale of GMCs, the iCOMs are likely tracing large-scale shocks, due to either cloud-cloud collision (1) or shocks related to star formation activity (scenario 2a; see also Huang et al. 2023). At pSSC scales, iCOMs could trace either star formation-related heating process (scenario 2b; CH_3NH_2, NH_2CHO) and shocks (scenario 2a; CH_3CHO, CH_2NH, C_2H_5OH), associated or not (i.e. if cloud-cloud collision, scenario 1) with star formation.

2020; De Simone et al. 2020; Vazart et al. 2020) or from C_2H_5OH (known as the 'ethanol tree'; e.g. Skouteris et al. 2018; Vazart et al. 2020). However, whilst the first pathway has been validated in both cold and warm environments, the validity of the second one has not been checked in cold environments (e.g. Vazart et al. 2020). Alternatively, various grain-surface reactions have been proposed for the formation of CH_3CHO (e.g. Bennett et al. 2005; Garrod et al. 2008; Ruaud et al. 2015; Lamberts et al. 2019; Barger & Garrod 2020; Martín-Doménech et al. 2020; Ibrahim et al. 2022), although the efficiency of some of these reactions has been debated (e.g. Rimola et al. 2018; Enrique-Romero et al. 2016, 2021). For C_2H_5OH, grain-surface reactions are mostly proposed but there is no consensus on the formation process (e.g. Jin & Garrod 2020; Chuang et al. 2020; Perrero et al. 2022; Enrique-Romero et al. 2022; Garrod et al.

2022; Molpeceres et al. 2024a). One of the proposed pathways involves CH_3CHO as a precursor (Bisschop et al. 2007; Chuang et al. 2020; Fedoseev et al. 2022), where it was expected that the solid-state abundances of C_2H_5OH would be lower than those of CH_3CHO (Sivaramakrishnan et al. 2009; Fedoseev et al. 2022). This formation pathway could be ruled out since recent observations made with the James Webb Space Telescope showed relatively similar ice abundances for the two species (Rocha et al. 2024; Chen et al. 2024), as found previously in the case of comets (Rubin et al. 2019). However, a direct comparison of the content seen in the ice and in the gas towards two low-mass protostars showed that this is not what is seen in the gas phase, where C_2H_5OH seems to be more abundant than CH_3CHO (Chen et al. 2024). On the other hand, gas phase reactions starting from $H_3O^+ + C_2H_4$ and leading to the formation of C_2H_5OH through $C_2H_5OH_2^+$ as a precursor have been

reported in both the KIDA[4] and UMIST[5] databases; thus, this could be a viable pathway if H_3O^+ is abundant enough (which may be the case due to the high CRIR towards these regions; e.g. Holdship et al. 2022; Behrens et al. 2024). In the following, we investigate whether ethanol (C_2H_5OH) and acetaldehyde (CH_3CHO) are correlated towards NGC 253.

Table B.2 on Zenodo shows that the mean FWHM and peak velocities of C_2H_5OH are generally more consistent with that of the colder component of CH_3CHO. Optical depth effects could alter these results but further similarities can be seen when looking at the column densities of the two species: From Figure 4, we see that both the column densities derived for GMC scales of C_2H_5OH and CH_3CHO are relatively constant throughout the four regions. In addition, their abundance ratio of ∼2.3 is also constant across the regions and show the best correlation at GMC scales (see Figure 6a). Therefore, a correlation between the cold component of CH_3CHO (governed by the low E_u transitions) and C_2H_5OH could indicate that the two species are chemically linked (see Fig. 7, hypothesis i). Since the abundance of C_2H_5OH is higher than that of CH_3CHO, the two species could be linked via the gas-phase production of CH_3CHO through the ethanol tree. This hypothesis, if true, implies that the ethanol tree pathway proposed by Skouteris et al. (2018) would also be valid at low temperatures, since the iCOMs are likely subthermally excited. On the other hand, we cannot rule out that the two species were formed on the grains before being ejected through shocked processes (see Sect. 5.2). The higher abundance of C_2H_5OH compared to that of CH_3CHO could then indicate more fast or important destruction or reprocessing of CH_3CHO in the gas phase compared to C_2H_5OH. For C_2H_5OH, one proposed formation path for its precursor $C_2H_5OH_2^+$ is via the gas phase reaction between H_3O^+ and C_2H_4. Considering the high CRIR derived towards NGC 253 (e.g. Holdship et al. 2022; Behrens et al. 2022), the abundance of H_3O_+ could be high enough for the gas phase production of ethanol to be viable.

When looking at the correlations at pSSC scales (see Figure 6f), the warm component of CH_3CHO (traced by the high E_u transitions) towards GMC 6 and pSSC 5 is no longer correlated with ethanol. The difference in peak velocity and FWHM for this high E_u transitions, compared to the low E_u transitions (see Table B.2 on Zenodo) indicates that additional CH_3CHO is produced in these two regions and likely through a different pathway. If the cold component of CH_3OH is formed in the gas phase, the warm CH_3CHO component could, on the other hand, form on the icy grain mantles via thermal desorption (if the gas temperature is high enough; see Sect. 5.2.2); alternatively, it could form via non-thermal processes such as shocks (e.g. Ruaud et al. 2015; Lu et al. 2025). We investigate the origin of the high excitation of CH_3CHO in GMC 6 and pSSC 5 in Sect. 5.3.

5.1.2. NH_2CHO

Both grain-surface formation (e.g. Raunier et al. 2004; Garrod et al. 2008; López-Sepulcre et al. 2015; Fedoseev et al. 2016; Rimola et al. 2018; Dulieu et al. 2019; Martín-Doménech et al. 2020; Chuang et al. 2022) and gas-phase formation (e.g. Kahane et al. 2013; Barone et al. 2015; Vazart et al. 2016; Skouteris et al. 2017) pathways have been suggested for formamide (NH_2CHO), but which is the most efficient is highly debated, as in the case of CH_3CHO. We refer to

López-Sepulcre et al. (2019) and López-Sepulcre et al. (2024) for a comprehensive review of the different formation paths proposed for formamide. Here, we only investigate the potential chemical link of NH_2CHO with HNCO and H_2CO, with both species thought to be chemically linked with NH_2CHO, either as a parent species on the ice grain mantle or in the gas phase (H_2CO; e.g. Fedoseev et al. 2016; Dulieu et al. 2019; Kahane et al. 2013; Vazart et al. 2016; Aikawa et al. 2020; López-Sepulcre et al. 2024) or as a daughter species (HNCO; Brucato et al. 2006; Gorai et al. 2020; Haupa et al. 2022; Chuang et al. 2022). Both H_2CO and HNCO were studied towards the CMZ of NGC 253 (Mangum et al. 2019; Huang et al. 2023, 2025).

Furthermore, HNCO traces low-velocity shocks throughout the CMZ of NGC 253 and the gas temperatures towards the four regions investigated in the present study range between ∼20 and 100 K (Huang et al. 2023). The rotational temperatures we derived range between ∼10−30 K and ∼50−80 K for the cold and warm component, respectively, consistent with that of HNCO. A word of caution is needed, however, since our rotational temperature could be underestimated if optical depth effects or NLTE effects are at play, as we found to be the case for CH_2NH (see Sect. 4.3). Using transitions with similar energy levels, we compared the emission distribution between NH_2CHO and HNCO around ∼40 and ∼140 K as shown in Appendix D (on Zenodo). NH_2CHO is much less intense compared to HNCO, as it is much less abundant, but the two species do not peak towards the same regions. This is also seen when comparing the derived column densities of NH_2CHO and HNCO: whilst HNCO has a relatively constant column density across the regions (Huang et al. 2023), the cold component of NH_2CHO decreases towards GMC 7, whilst the warm component is lower towards pSSC 2. Neither of the two component of NH_2CHO seem thus to be chemically linked with HNCO.

As for HNCO, we also compared the emission distribution of NH_2CHO and H_2CO at similar energy levels, around 45 and 100 K, as shown in Appendix D (on Zenodo). Even though NH_2CHO is much less intense than H_2CO due to its lower abundance, we can see a good correlation between the two species at low E_u with a peak of emission towards GMC 6 and pSSC 5. Therefore, the cold component of NH_2CHO and H_2CO could be chemically linked: H_2CO being likely a gas phase product (Huang et al. 2025), NH_2CHO would thus form in the gas phase, from the reaction $H_2CO + NH_2$ (Kahane et al. 2013; Barone et al. 2015; Vazart et al. 2016; López-Sepulcre et al. 2024). However, this scenario is challenged by the different temperatures traced by the two species since the rotational temperature for the cold component of NH_2CHO is less than 30 K, while H_2CO was found to trace a warmer gas ($T_{kin} \geq 70$ K at scales 1.6–5″ scales and $T_{kin} \geq 300$ K at scales ≤ 1″; Mangum et al. 2019; Huang et al. 2025). The low temperature of NH_2CHO could result from subthermal excitation. Unless the T_{rot} values are underestimated, we cannot conclude whether NH_2CHO and H_2CO are chemically linked and whether the cold component of NH_2CHO is a gas-phase or a grain-surface product.

On the other hand, the difference of peak velocities and FWHM for the low and high E_u transitions (see Figure 3) could indicate that NH_2CHO truly traces two different gas components. Indeed, this warmer ($T_{rot} > 50$ K) component, clearly present in GMC 6 and pSSC 2, shows a narrower mean FWHM, compared to the cold gas component and warmer rotational temperatures (see Figure 4). Hence, another formation pathway could be involved for the warm component of NH_2CHO,

---

[4] https://kida.astrochem-tools.org/
[5] https://umistdatabase.net/

different from that of the cold component. As for CH_3CHO, we further investigate the origin of this emission in Sect. 5.3.

5.1.3. CH_2NH and CH_3NH_2

From the literature, CH_3NH_2 is proposed to form on the ice grain surfaces through radical-radical reactions (e.g. Garrod et al. 2008; Kim & Kaiser 2011; Förstel et al. 2017; Enrique-Romero et al. 2022) or from the successive hydrogenation of CH_2NH (e.g. Woon 2002; Theule et al. 2011; Sil et al. 2018; de Jesus et al. 2021; Molpeceres et al. 2024b). Whilst the first pathways overpredicts CH_3NH_2 abundances (Garrod et al. 2008), the second possible pathway has been supported by chemical models reproducing observed abundances of CH_3NH_2 towards high-mass protostars (Suzuki et al. 2016, 2023). This second pathway would indicate that CH_2NH is a precursor of CH_3NH_2 and would also form on the ice grain mantles. However, studies have shown that the conversion of CH_2NH to CH_3NH_2 would be too fast to account for the gas phase abundance of CH_2NH (e.g. Theule et al. 2011; Suzuki et al. 2016). In addition, Molpeceres et al. (2024b) very recently proposed a grain-surface formation route for CH_3NH_2 from the CNH_3 chemisorbate, without passing through CH_2NH as an intermediate species. From the recent literature, it does seem that the two species are not necessarily chemically linked (as had been previously assumed). Alternatively from the grain-surface production, the neutral–neutral gas phase reaction $CH_3 + NH_3 \rightarrow CH_3NH_2 + H$ has also been proposed as a viable formation pathway in warm ($T > 100$ K) regions (Bocherel et al. 1996; Halfen et al. 2013). Similarly for CH_2NH, various gas-phase formation pathways (ion-molecules or neutral-neutral reactions involving CH_3 or NH_3; see e.g. Table 11 of Suzuki et al. 2016) have been proposed as a viable alternative for the formation of CH_2NH (e.g. Bocherel et al. 1996; Turner et al. 1999; Suzuki et al. 2016; Sil et al. 2018).

From Table B.2 (see Zenodo), both the peak velocities and FHWM of CH_2NH and CH_3NH_2 are consistent with each other (and considering the spectral resolution of $10 \, km \, s^{-1}$) in all the four regions investigated. From the RDs, we found similar rotational temperatures between CH_2NH and the warm component of CH_3NH_2 in all the regions – except GMC 6 (see Figure 4); however, it was shown that temperatures were underestimated in the case of CH_2NH. For the column densities, since CH_2NH was found to emit at smaller scales than GMC scales (see Sect. 4.3), we compared the column densities of CH_2NH and of the warm component of CH_3NH_2 at pSSC scales only. From Figure 4, the column densities of the warm component of CH_3NH_2 and of CH_2NH are relatively constant across the regions, as seen also in their abundance ratio: Figure 6 shows a very good correlation (panel e) between CH_2NH and the cold component of CH_3NH_2, whilst the correlation becomes weaker (high p-value, panel j) correlation between CH_2NH and the warm component of CH_3NH_2. This weak correlation might be due to the slight decrease in the abundance ratio towards GMC 6, which seems to come from a higher column density in CH_2NH. However, the LVG results did not confirm this increase in CH_2NH towards GMC 6 and the correlation between the two species could be strong for both components of CH_3NH_2.

If the correlation between CH_2NH and CH_3NH_2 is true, the two species could be chemically linked (see Fig. 7, hypothesis ii). Since the grain formation pathways linking CH_3NH_2 and CH_2NH are not viable to explain gas-phase abundance of CH_2NH (see above), the two species can be chemically linked if they share the same precursor. On the grain, the new proposed formation route of the two species from CNH_3 indicates that both species can have HCN and HNC as precursors, without CH_2NH being a precursor of CH_3NH_2. In the gas phase, formation pathways involving CH_3 and NH_3 are viable for both species but only for temperatures above 100 K. Hence, should the two species be chemically linked, both grain-surface and gas-phase reactions could account for the correlation and the chemical link. Our current results, however, do not allow us to distinguish between the two possibilities. Alternatively, the correlation could indicate that the two species trace similar physical processes of formation across the various regions (e.g. Quénard et al. 2018; Belloche et al. 2020).

5.2. Possible origins of the iCOMs in the CMZ of NGC 253

In the previous section, we discussed the iCOMs possible formation pathways and whether any pair of iCOMs has a chemical link. We discuss below the physical process that could be responsible for the iCOMs emission towards the CMZ of NGC 253.

A first inspection of the emission distribution of the iCOMs in this study shows that the emission is (1) mostly concentrated towards the inner part of the CMZ, within 6″ around the kinematic centre, (2) compact around each GMC, and (3) sometimes unresolved for the higher upper-level energies, depending the species. From the images, we thus hypothesize that the emission could be emitted on GMC scales (of the size of the order of the ALCHEMI beam size or 1.6″) and unresolved pSSC scales (~0.12″ or a few parsecs), which are the next biggest substructures identified within the GMCs (e.g. Ando et al. 2017; Leroy et al. 2018). As we could not derive the emission size of the iCOMs (except for CH_2NH) we discuss how they would be produced at GMC and pSSC scales (Sects. 5.2.1 and 5.2.2, respectively) in the following.

5.2.1. iCOMs production at GMC-scales

Several studies derived the volume density and kinetic temperature of the molecular gas in the disk of NGC 253, and found at least two components (e.g. Rosenberg et al. 2014; Gorski et al. 2017; Pérez-Beaupuits et al. 2018; Mangum et al. 2019; Tanaka et al. 2024). The most recent study by Tanaka et al. (2024) derived a gas temperature and density for the low-density component (dominated by the low-J lines of CO and its isotopologues) of 85 K and $2 \times 10^3 \, cm^{-3}$, respectively, and for the high-density component (dominated by high-density tracers with $E_u \leq 70$ K) of 110 K and $\sim 3 \times 10^4 \, cm^{-3}$, respectively. Their results are consistent with previous studies. The dust temperatures were also estimated to be around 35–40 K (Leroy et al. 2015; Martín et al. 2021). Leroy et al. (2015) derived line widths for the GMCs of NGC 253 of $\sim 20-40 \, km \, s^{-1}$ using observations of bulk gas tracers (e.g. low-J lines of CO, HCN, HCO^+, and isotopologues).

On average, the derived rotational temperatures ($T_{rot} \leq 60$ K) for the iCOMs are thus below the gas temperatures found at GMC scales. At the densities measured (i.e. $n_{H_2} \sim 10^3-10^4 \, cm^{-3}$), the dust and gas are likely not coupled. Most recent laboratory experiments and quantum chemical calculations of binding energies showed that CH_3CHO and CH_3NH_2 would desorb at a lower dust temperature than water (~100−120 K; Chaabouni et al. 2018; Ferrero et al. 2022; Molpeceres et al. 2022), whilst C_2H_5OH would co-desorb with water at around 140 K (Perrero et al. 2024). On the other hand, NH_2CHO is refractory to water desorption and would desorb at higher dust temperatures (≥170−300 K; e.g.

Urso et al. 2017; Chaabouni et al. 2018; Ligterink et al. 2018; Martín-Doménech et al. 2020; Ferrero et al. 2020; Chuang et al. 2022). Therefore, the dust temperature derived at GMC scales (35–40 K) is too low to desorb the iCOMs, if they formed on the icy grain mantles. The iCOMs are very likely sub-thermally excited and are released into the gas phase via non-thermal processes if they formed on the grains. With the CRIR being relatively high ($\zeta \sim 10^{-14}-10^{-12}$ s^{-1}; e.g. Holdship et al. 2022; Behrens et al. 2022, 2024) towards the CMZ of NGC 253, CR-induced grain heating and sputtering desorption mechanisms (e.g. Roberts et al. 2007; Dartois et al. 2019; Paulive et al. 2022; Arslan et al. 2023) could be an important process in desorbing these iCOMs.

Another important non-thermal process in NGC 253 working to release the species from the ice grain mantles into the gas phase could be shock sputtering. In this work, we measured average line widths of mostly around 40–60 km s^{-1} (see Table B.2 on Zenodo) for the cold gas component (component 1) of the iCOMs. These values are on average larger than the line widths derived by Leroy et al. (2015) for the GMCs (between 20 and 40 K), which could indicate that the species trace a more turbulent gas. However, as mentioned earlier in this paper, we cannot exclude possible optical depth effects, as is the case for CH$_2$NH. If we considered moderate to high optical depth ($\tau \sim 0.6-3$) as we found for CH$_2$NH, we could end up overestimating the line widths between 12% and 30%[6]. In the most optically thick case derived ($\tau = 3$), for a FWHM of 60 km s^{-1}, the opacity-corrected line width would still be above that of GMCs; however, this would not be the case for a FWHM of 40 km s^{-1}.

O-bearing iCOMs: From Sect. 5.1.1, we found that CH$_3$CHO and C$_2$H$_5$OH could be chemically linked. If this is the case, then the cold component of CH$_3$CHO could be produced in the gas phase from C$_2$H$_5$OH, which would have been sputtered from the grain through shocks. Alternatively, both species could be formed on the grain and be linked with CH$_3$CHO as a precursor of C$_2$H$_5$OH (e.g. Chuang et al. 2020; Fedoseev et al. 2022), but the gas phase abundance ratio would not be representative of the ice abundances (see Sect. 5.1.1). In any case, CH$_3$CHO and C$_2$H$_5$OH tracing shocks would be consistent with the fact that both species are detected in protostellar shocks in our Galaxy (e.g. Arce et al. 2008; Lefloch et al. 2017; Holdship et al. 2019; Csengeri et al. 2019; Codella et al. 2020; De Simone et al. 2020; Busch et al. 2024).

N-bearing iCOMs, including NH$_2$CHO: Since NH$_2$CHO has not been detected in cold clouds (López-Sepulcre et al. 2019) and the rotational temperatures for the cold component are low (<30 K) enough to point to sub-thermal excitation, the cold component of NH$_2$CHO is also very likely to be tracing shocked gas. This would be consistent with what is seen and modelled in Galactic shocked regions (e.g. Arce et al. 2008; Burkhardt et al. 2019; Codella et al. 2017; López-Sepulcre et al. 2024). The correlation of CH$_3$NH$_2$ with NH$_2$CHO at GMC scales (see Figure 6d) could indicate similar physical conditions across these regions for the formation environment of the two species (e.g. Quénard et al. 2018; Belloche et al. 2020), since no chemi-

cal reaction linking the two species has been reported in the literature. On the other hand, we found that CH$_3$NH$_2$ and CH$_2$NH could be chemically linked or could trace the same physical process (see Sect. 5.1.3). Therefore, CH$_3$NH$_2$ and CH$_2$NH are also very likely tracing shocked gas. Recently, Zeng et al. (2018) found abundant N-bearing species towards G+0.693-0.027, a molecular cloud in the GC. They mentioned that the rich chemistry of this source is due to the fact that it is dominated by low-velocity shocks and the high cosmic-ray ionisation rates (Rivilla et al. 2022a; Sanz-Novo et al. 2024). They reported a ratio [CH$_3$NH$_2$]/[NH$_2$CHO] and [CH$_3$NH$_2$]/[CH$_2$NH] of 5, which is of the same order of magnitude as our value of ~3 for both ratios.

Overall, at GMC scales, sputtering due to large-scale shocks is likely the main process releasing the iCOMs into the gas phase. Signatures of shocks have been previously found within the CMZ of NGC 253 were already found in previous studies towards NGC 253 (e.g. García-Burillo et al. 2000; Meier et al. 2015; Haasler et al. 2022; Harada et al. 2022; Huang et al. 2023). Large-scale shocks traced by iCOMs would also be consistent with the origin of CH$_3$OH, the simplest iCOM, which is also tracing shocks within NGC 253 (e.g. Humire et al. 2022; Huang et al. 2025). We compared the emission distribution of CH$_3$OH with that of CH$_3$CHO and CH$_3$NH$_2$ around $E_u = 20$ K and found a relatively good correlation – except towards GMC 7, where we retrieved the O- vs N- disparity. The contour maps of the above-mentioned transitions are shown in Appendix D (Zenodo). Following the possible shock scenarios by Huang et al. (2023), as seen in their Figure 12 in particular, the shocks traced by the iCOMs could be due to either star-formation within each GMC (via shocks induced by outflows or sporadic shocks due to scattered star-formation episodes; see scenario 2a in Figure 7) or cloud-cloud collisions (see scenario 1 in Figure 7).

The intersection of different orbits (such as Lindblad resonances; Iodice et al. 2014) can lead to large-scale cloud–cloud collisions (see Harada et al. 2022; Humire et al. 2022 and references therein). However, the regions we observe are not located close to such intersections, which indicates that the large-scale shocks traced by the iCOMs are either due to cloud-cloud collisions occurring within the GMCs (scenario 1 in Figure 7) or to star formation activity (scenario 2a in Figure 7). From the LVG analysis, we found that CH$_2$NH is emitted on size scales between 0.15″ and 0.6″, which corresponds to 2.5–10 pc in linear scales, supporting the large-scale shocks scenario within GMCs. The situation could resemble that of our Galactic centre, where the widespread emission of iCOMs is detected throughout the CMZ and are likely caused by low-velocity shocks due to cloud-cloud collisions (e.g. Requena-Torres et al. 2006; Jones et al. 2011; Li et al. 2017, 2020; Zeng et al. 2020). Therefore, chemical modelling will help disentangle between the different shock scenarios. Finally, both O- and N-bearing iCOMs are well correlated – except towards GMC 7, where O-bearing species are more abundant than N-bearing species. We discuss this further in Sect. 5.3.1.

5.2.2. iCOMs production at pSSC-scale

The previously derived temperatures of the pSSCs are ≥100 K (Rico-Villas et al. 2020; Krieger et al. 2020). The PSSCs show clear outflow features (Gorski et al. 2019; Levy et al. 2021), and some of them host super-hot cores (SHCs; Rico-Villas et al. 2020) from the detection of vibrationally excited HC$_3$N emission and densities and temperatures of ~10^6 cm^{-3} and ~200−300 K,

---

[6] Using the formula $\sigma_{\mathrm{obs}} = \frac{\sigma_0}{\sqrt{\ln 2}} \sqrt{\ln\left(\frac{\tau}{\ln\left(\frac{2}{1+e^{-\tau}}\right)}\right)}$ with σ_{obs}, σ_0 and τ_ν the observed and intrinsic velocity dispersions, and the line opacity, respectively (Burton et al. 1992). The velocity dispersion (σ_ν) is linked to the FWHM by $\sigma_\nu = \mathrm{FWHM}/2\sqrt{2\ln(2)}$.

respectively. Such high temperatures are consistent with the kinetic temperatures derived at scales ≤1″ (≤17 pc) using H_2CO observations (Mangum et al. 2019). The densities of the pSSCs are high enough to consider that the dust and gas are coupled. Therefore, the gas temperature at pSSC scales would be enough to thermally desorb the iCOMs (Scenario 2b in Figure 7), should they be formed on grains. Sputtering from shocks due to outflows driven by the stars undergoing formation is also a possible mechanism behind the release of iCOMs into the gas phase or, alternatively, this could lead to a rich gas-phase chemistry, enabling the formation of iCOMs (Scenario 2a in Figure 7).

As for the GMC scales, the rotational temperatures derived for the iCOMs are much lower ($T_{rot} \leq 60$ K) than the gas temperature we expect at pSSCs scales, which could indicate that they are tracing a less dense gas. Therefore, we can see that the iCOMs are very likely sub-thermally excited on pSSC scales as well. Due to the limited temperature range for which the collisional rates were calculated, we could not constrain the upper limit of the gas kinetic temperature – except for GMC 6, where the range is $T_{rot} = 25-130$ K (see Sect. 4.3). Suzuki et al. (2016) estimated an upper limit for the desorption temperature of CH_2NH of 160 K, consistent with the mean binding energy of 5534 K derived by Ruaud et al. (2015). If all the iCOMs are tracing the same gas component, then C_2H_5OH and NH_2CHO in GMC 6 cannot be thermally desorbed if they formed on the grain. However, higher temperatures derived in the other regions could indicate that thermal desorption is indeed at work.

O-bearing iCOMs: Both CH_3CHO and C_2H_5OH have been detected in shocked regions associated with outflows from protostars (e.g. Arce et al. 2008; Lefloch et al. 2017), as well as the warm envelope of protostars (e.g. Belloche et al. 2013; Fuente et al. 2014; Jørgensen et al. 2018; Bonfand et al. 2019; Lee et al. 2019; Gorai et al. 2024; Möller et al. 2025). The abundance ratio [C_2H_5OH]/[CH_3CHO] ranging between ~2.3−5 (see Figure 6f) corresponds well to the abundance ratio found in low- and high-mass star-forming regions, as well as to shocks linked to protostellar outflows (e.g. Lefloch et al. 2017; Chen et al. 2023; Busch et al. 2024).

N-bearing iCOMs, including NH_2CHO: The measured abundance ratio of [CH_3NH_2]/[NH_2CHO] = 3−10 towards GMC 7 and pSSC 5 (see Figure 6i) is similar to the ratios measured in high-mass protostars (Bøgelund et al. 2019b; Nazari et al. 2022). The highest ratios derived towards GMC 6 and pSSC 2 (5 and 10, respectively) are in line with the range of values predicted by the chemical models of hot cores by Garrod et al. (2022) (see their Table 19). The increase in the abundance ratio is due to the smaller column density of NH_2CHO in these regions (see Figure 4). We investigate possible physical causes in Sect. 5.3 below. Finally, the abundance ratio between the warm component of CH_3NH_2 and CH_2NH is close to 3 in all four regions (see Figure 6j), which falls on the lower side of ratios measured in massive protostars (Bøgelund et al. 2019b and references therein, Suzuki et al. 2023). When comparing to the hot core models by Garrod et al. (2022), our measured ratios are well below those predicted by the model (see their Table 17). The discrepancy could arise from the lack of destruction routes of CH_3NH_2 in the model (Garrod et al. 2022). To the best of our knowledge, between the two species, only CH_2NH has been detected in shocked or outflowing regions (e.g. Widicus Weaver et al. 2017; Gorski et al. 2023). From the PCA analysis performed by Harada et al. (2024), CH_2NH was corre-

lated with both shock tracers (SiO) and high-energy transitions of HC_3N, thought to be linked with young starbursts. The warm compact component of CH_3NH_2 could not probe the same gas component as CH_2NH, which can be partially supported by the weak correlation between the two species (see Figure 6).

Overall, if iCOMs are emitted on pSSC scales, the gas could be warm enough to desorb those forming on the icy grain mantles (scenario 2b in Fig. 7). Alternatively iCOMs could be tracing shocks, associated (scenario 2a in Fig. 7) or not (scenario 1 in Fig. 7) with ongoing star formation. With our current angular resolution, we cannot really distinguish between the different scenarios. Higher angular resolution observations and chemical modelling will be necessary to distinguish between the various processes.

5.3. Chemical variations across regions

In the sections above, we found some chemical differences between the four regions. On the one hand, we found that GMC 7 presents an enhancement in O-bearing species compared to N-bearing species. On the other hand, we found that whilst high E_u transitions of CH_3CHO are excited only towards GMC 6 and pSSC 5, those for NH_2CHO are excited in GMC 6 and pSSC 2, indicating an anti-correlation between the two species towards pSSC 5 and pSSC 2. The H_2 density between the four regions does not seem to change significantly based on previous studies on various molecular tracers (e.g. Behrens et al. 2022; Huang et al. 2023; Bouvier et al. 2024). Hence, the chemical differentiation seen could be real and we investigate its possible causes below.

5.3.1. The O- versus N-bearing dichotomy towards GMC 7

The contour maps in Figure 1 and the correlation plots in panels b, c, g, and j of Figure 6 show a dichotomy between the O and N-bearing species toward GMC 7. Looking at Table B.2 (see Zenodo), there is no particular shift in V_{peak} or change in FWHM between N- and O-bearing iCOMs towards GMC 7 which would highlight a different origin of emission between the two types of iCOMs. If we consider the column densities derived at GMC scales (see bottom part of Figure 4), GMC 7 shows a decrease in N-bearing species compared to the other regions, whilst the amount of O-bearing species stay relatively constant. Thus, we consider what causes the lack of N-bearing species towards GMC 7, compared to the other regions.

A first factor could be related to a difference in physical conditions in this GMC. In Sect. 5.2.1, we hypothesised that most of the iCOMs could be linked to shocks occurring within the GMCs. From the analysis of shock species (e.g. HNCO, SiO, and S-bearing species; Huang et al. 2023; Bouvier et al. 2024), it was shown that shocks are likely less intense towards GMC 7 compared to the other regions. Stronger shocks would lead to the presence of warmer gas. However, from the gas temperatures derived for CH_2NH in Sect. 4.3, GMC 7 does not show a clear temperature difference compared to the other regions. On the other hand, the H_2 column density in GMC 7 is lower compared to the other three regions by approximately one order of magnitude (e.g. Mangum et al. 2019). A correlation between the amount of formed iCOMs and the H_2 column density was found in low-mass and high-mass protostellar cores, indicating that iCOMs formation is more advanced in denser cores (Yang et al. 2021; Baek et al. 2022). However, in Baek et al. (2022), whilst the abundance of CH_3CHO was found to be relatively constant with N_{H_2}, the abundances of C_2H_5OH, CH_3NH_2, and NH_2CHO

were found to grow proportionally with N_{H_2}. Hence, the difference in column density does not seem to explain the O- vs. N-dichotomy.

A second factor leading to a difference in O- versus N-bearing iCOMs could be evolutionary. Huang et al. (2023) estimated a timescale for the history of the shocks for each GMC and suggested that shocks towards GMC 7 are older ($\sim 10^4$ yr) than shocks towards the three other GMCs ($\sim 10^3$ yr). Hence, the lower abundance in N-bearing species, if they are all tracing the same shock event, could be linked to the fact that the shock is older. However, this would contradict what is observed in the Galactic prototypical L1157-B1 shock. There, an anti-correlation between CH_3CHO and NH_2CHO was observed (Codella et al. 2017), but the authors showed that CH_3CHO was tracing the youngest shock, whilst NH_2CHO is shown to be tracing the older part of the shock, as the species needs time to be formed in the gas phase. We would thus have expected GMC 7 to be more abundant in N-bearing species if it had been tracing older shocks – however, this is not the case. We should note that the timescale estimation of the shocks in the GMCs of NGC 253 relies on the assumption that both HNCO and SiO are tracing the same shock episode, which is not necessarily the case.

Studies of high-mass star-forming regions have shown that less evolved sources have a lower amount of N-bearing iCOMs, compared to O-bearing ones (e.g. Beuther et al. 2009; Suzuki et al. 2018; Bøgelund et al. 2019a; Baek et al. 2022). This is explained by the fact that ice or gas-phase nitrogen chemistry takes longer to initiate compared with the chemistry of O-bearing species (e.g. Charnley et al. 1992; Beuther et al. 2009; Garrod et al. 2022). Interestingly, Dedes et al. (2011) observed three high-mass star-forming regions and found an overabundance of O-bearing species compared to N-bearing ones. However, whilst one of the sources is very young, the other two are relatively evolved with HII regions. Hence, a low N-bearing iCOM abundance does not necessarily imply a younger region. In addition, it is not known whether pSSCs are present within GMC 7, as it was not included in Ando et al. (2017) and Leroy et al. (2018). Understanding the core population could bring additional information on whether the GMC is younger or older compared to the other GMCs. Observations of radio recombination lines (RRLs) and 3 mm continuum emission (due to free-free emission), both arising from ionised gas that traces ongoing star formation, showed that while there is no clear RRL emission towards GMC 7, faint 3 mm continuum has been detected (e.g. Rodríguez-Rico et al. 2006; Bendo et al. 2015). In addition, only one radio continuum source (unclassified) has been identified in the vicinity of GMC 7, in contrast to the other three regions (Ulvestad & Antonucci 1997). Young star formation could thus be much less active towards GMC 7, which is supported by the lack of line emission usually associated with young starburst towards this region (Harada et al. 2024; Kishikawa et al. 2025). Finally, performing chemical modelling will also be essential to help us understand the lack of N-bearing species towards GMC 7.

5.3.2. The CH_3CHO – NH_2CHO excitation condition anti-correlation in pSSC 5 and pSSC 2

The regions GMC 6, pSSC 5, and pSSC 2 show a relatively similar chemical content in terms of iCOMs. There is, however, a small difference between pSSC 5 and pSSC 2, when it comes to the warmer and more compact component (governed by high E_u transitions) that we identified in the rotational diagram analysis (see Sect. 4.2). Indeed, whilst NH_2CHO transitions with E_u up

to 200 K are detected towards GMC 6 and pSSC 2, it is not the case towards pSSC 5. On the other hand, the situation is reversed for CH_3CHO, where high E_u transitions, up to 80–100 K, are lacking towards pSSC 2. We investigate below whether known differences between these two regions could explain the lack of high excitation transitions for these two species.

Since the chemical difference concerns transitions for which the emission is mostly unresolved by the ALCHEMI beam, we consider that the difference might come from the small-scale constitution of the GMCs, namely, at pSSC scales. Our ALCHEMI beam encompasses several of the pSSCs identified by Leroy et al. (2018). Our regions pSSC 5 and pSSC 2 encompass pSSCs 4–7 and pSSCs 1–3, respectively. In the case of GMC 6, only one pSSC has been identified (pSSC 14). The pSSC's chemical richness and physical properties have been investigated by a few studies at high angular resolution (e.g. Krieger et al. 2020; Levy et al. 2021; Mills et al. 2021). From these studies, no significant differences in the chemical composition have been found towards the pSSCs that would be of interest to this work. Additionally, all host SHCs so the difference is likely not coming from a difference in source population between the pSSCs. On the other hand, only pSSC 14, pSSC 4, and pSSC 5 show clear outflow features (Levy et al. 2021). If, on the scales of pSSCs, CH_3CHO and NH_2CHO do not probe the same gas component, then we could explain the lack of high excitation transitions of CH_3CHO towards our region pSSC 2 if CH_3CHO traces shocked gas linked to the pSSC's outflow; whilst NH_2CHO traces the forming pSSCs themselves. If NH_2CHO is linked to the pSSCs and their hosting SHCs, then a difference between the properties of the sources is needed to explain the lack of high excitation of the species towards pSSC 5. Looking at the gas temperature derived for the SHCs (Rico-Villas et al. 2020), the pSSCs composing our region pSSC 5 seem to have a slightly lower temperature compared to those of regions GMC 6 and pSSC 2. As already mentioned, due to the binding energy range of NH_2CHO being the highest among the iCOMs studied here, the region pSSC 5 could thus be less efficient in releasing NH_2CHO if it forms on the grain. Moreover, a cooler gas temperature could indicate younger source, which would then suggest that the pSSC 5 is younger than the two others. However, there is no clear consensus on the evolutionary age pattern of the pSSCs (e.g. Rico-Villas et al. 2020; Krieger et al. 2020; Mills et al. 2021; Levy et al. 2021). Furthermore, this hypothesis does not explain why narrower line widths for NH_2CHO are detected solely towards pSSC 2.

6. Conclusions

We used ALCHEMI ALMA large programme measurements to investigate the emission and formation pathways of selected iCOMs, CH_3CHO (acetaldehyde), C_2H_5OH (ethanol), NH_2CHO (formamide), CH_2NH (methanimine), and CH_3NH_2 (methylamine), towards the CMZ of NGC 253. We performed radiative transfer analyses to derive rotational temperatures and column densities for each iCOM under study. For CH_2NH, we performed a NLTE LVG analysis as this was the only iCOM in our study with available collisional rates. We studied the relation between the iCOMs at both GMC and pSSC scales, to see whether chemical and physical differences between iCOMs and regions are present. We also examined how it could relate to the source's physical or chemical structure. We summarise our main findings below.

- The iCOM emission is mostly concentrated towards the inner part of the CMZ (i.e. within 6″ or $\sim$100 pc around

the kinematic centre), between GMC 7 and pSSC 2 (close to GMC 3). At a similar upper-level energy, we find that CH$_2$NH and CH$_3$NH$_2$ are usually more spatially extended, compared to CH$_3$CHO, C$_2$H$_5$OH, and NH$_2$CHO. Finally, emission from iCOMs becomes more compact with increasing E_u

- A rotational diagram analysis showed that for CH$_3$NH$_2$, CH$_3$CHO and NH$_2$CHO, two gas components are needed depending on the region, for which we applied two different beam-filling factors, one for a region of emission at the scale of GMCs and the other at the scale of pSSCs.

- All T_{rot} derived are below 100 K and the majority lie in the range $10 - 40$ K, indicating that iCOMs are sub-thermally excited. The column densities of CH$_3$CHO and C$_2$H$_5$OH are relatively constant throughout the regions. The N-bearing species, on the other hand, show a decrease towards GMC 7.

- The LVG analysis we performed on CH$_2$NH shows that both optical depths and NLTE effects are at play for this species. The derived gas temperature and density show that CH$_2$NH emits in a gas of at least 20 K and at a density of 6×10^4 cm^{-3} for GMC 7, and up to 6×10^6 cm^{-3} for GMC 6. The emission size of CH$_2$NH is more compact than GMC scales ($\sim 0.15'' - 0.6''$ or $\sim 2.5 - 10$ pc).

- The cold extended components of CH$_3$CHO ($E_u < 40$ K) and C$_2$H$_5$OH are well correlated in all four regions, which could imply a chemical link between the two species. Gas phase production of CH$_3$CHO from C$_2$H$_5$OH through the 'ethanol tree' could be possible, although we cannot exclude grain formation for the two species.

- The cold extended component of NH$_2$CHO ($E_u < 70$ K) and H$_2$CO have similar peak of emission within the CMZ of NGC 253. If the two species are chemically linked (as proposed in the literature), then NH$_2$CHO could have formed in the gas phase via the reaction H$_2$CO + NH$_2$.

- Both gas components of CH$_3$NH$_2$ are well correlated with CH$_2$NH, respectively, which could indicate that they are either tracing a similar physical process or that they formed through the same precursor on the ice grain mantle or in the gas phase. Our current results do not allow us to draw a definitive conclusion between the two possibilities.

- If the iCOMs emit at GMC scales, the most favourable scenario to explain the widespread emission of the iCOMs is if they are tracing large-scale shocks within the GMCs. This resembles what is seen in the centre of our own Galaxy.

- Part of the iCOM emission may come from smaller scales, such as pSSC scales. Both thermal and non-thermal desorption may be thus at play, due to the heating from stars undergoing formation. Not all iCOMs may trace the same gas component, some of them likely tracing heating processes (e.g. CH$_3$NH$_2$, NH$_2$CHO) whilst the others may rather trace shock processes due to active star formation (e.g. CH$_2$NH, CH$_3$CHO, C$_2$H$_5$OH). We cannot, however, draw any firm conclusions on the origin of the iCOMs at pSSC scales without higher angular resolution or chemical modelling.

- At GMC scales (governed by a cold extended component of the iCOMs), GMC 7 shows a deficiency in N-bearing iCOMs compared to the other regions. The cause may be a different evolutionary stage of GMC or due to the simple fact that star formation is less active in that region.

- pSSC 5 and pSSC 2 show different excitation conditions for CH$_3$CHO and NH$_2$CHO. Whilst NH$_2$CHO does not have a warm component towards pSSC 5, CH$_3$CHO does not have a warm component towards pSSC 2. The difference could be partially explained if the two species are tracing different features, with CH$_3$CHO tracing the outflows driven by the pSSCs and NH$_2$CHO tracing the heating sources. However, we cannot explain the significant narrow line widths of NH$_2$CHO that are solely present towards pSSC 2.

This first study of iCOMs towards the CMZ of NGC 253 shows that several processes could be involved in their emission. The current angular resolution allows us to put some constraints on the region of emission of the iCOMs and their formation pathways; however, chemical modelling and higher angular resolution observations will be crucial to address all the questions raised in this work. In addition, while Galactic studies at high angular resolution help precisely determine where iCOMs are emitted, this remains a challenge with respect to extragalactic studies.

Data availability

Appendices B to D are publicly available on Zenodo: https://doi.org/10.5281/zenodo.15323347.

References

Aikawa, Y., Furuya, K., Yamamoto, S., & Sakai, N. 2020, ApJ, 897, 110
Ando, R., Nakanishi, K., Kohno, K., et al. 2017, ApJ, 849, 81
Arce, H. G., Santiago-García, J., Jørgensen, J. K., Tafalla, M., & Bachiller, R. 2008, ApJ, 681, L21
Arslan, Ö., Hocuk, S., Caselli, P., & Küçük, İ. 2023, MNRAS, 518, 2050
Baek, G., Lee, J.-E., Hirota, T., Kim, K.-T., & Kim, M. K. 2022, ApJ, 939, 84
Barger, C. J., & Garrod, R. T. 2020, ApJ, 888, 38
Barone, V., Latouche, C., Skouteris, D., et al. 2015, MNRAS, 453, L31
Behrens, E., Mangum, J. G., Holdship, J., et al. 2022, ApJ, 939, 119
Behrens, E., Mangum, J. G., Viti, S., et al. 2024, ApJ, 977, 38
Belloche, A., Müller, H. S. P., Menten, K. M., Schilke, P., & Comito, C. 2013, A&A, 559, A47
Belloche, A., Garrod, R. T., Müller, H. S. P., et al. 2019, A&A, 628, A10
Belloche, A., Maury, A. J., Maret, S., et al. 2020, A&A, 635, A198
Bendo, G. J., Beswick, R. J., D'Cruze, M. J., et al. 2015, MNRAS, 450, L80
Bennett, C. J., Jamieson, C. S., Osamura, Y., & Kaiser, R. I. 2005, ApJ, 624, 1097
Beuther, H., Zhang, Q., Bergin, E. A., & Sridharan, T. K. 2009, AJ, 137, 406
Bianchi, E., Codella, C., Ceccarelli, C., et al. 2019, MNRAS, 483, 1850
Bianchi, E., López-Sepulcre, A., Ceccarelli, C., et al. 2022, ApJ, 928, L3
Bisschop, S. E., Fuchs, G. W., van Dishoeck, E. F., & Linnartz, H. 2007, A&A, 474, 1061
Blake, G. A., Sutton, E. C., Masson, C. R., & Phillips, T. G. 1987, ApJ, 315, 621

Bocherel, P., Herbert, L., Rowe, B., et al. 1996, JPhCh, 100, 3063
Bøgelund, E. G., Barr, A. G., Taquet, V., et al. 2019a, A&A, 628, A2
Bøgelund, E. G., McGuire, B. A., Hogerheijde, M. R., van Dishoeck, E. F., & Ligterink, N. F. W. 2019b, A&A, 624, A82
Bonfand, M., Belloche, A., Garrod, R. T., et al. 2019, A&A, 628, A27
Bouscasse, L., Csengeri, T., Wyrowski, F., Menten, K. M., & Bontemps, S. 2024, A&A, 686, A252
Bouvier, M., Viti, S., Behrens, E., et al. 2024, A&A, 689, A64
Brucato, J. R., Baratta, G. A., & Strazzulla, G. 2006, A&A, 455, 395
Burkhardt, A. M., Shingledecker, C. N., Le Gal, R., et al. 2019, ApJ, 881, 32
Burton, W. B., Elmegreen, B. G., Genzel, R., et al. 1992, Saas-Fee Advanced Course 21: The Galactic Interstellar Medium
Busch, L. A., Belloche, A., Garrod, R. T., Müller, H. S. P., & Menten, K. M. 2024, A&A, 681, A104
Caselli, P., Hasegawa, T. I., & Herbst, E. 1993, ApJ, 408, 548
Ceccarelli, C., Maret, S., Tielens, A. G. G. M., Castets, A., & Caux, E. 2003, A&A, 410, 587
Ceccarelli, C., Caselli, P., Fontani, F., et al. 2017, ApJ, 850, 176
Ceccarelli, C., Codella, C., Balucani, N., et al. 2023, in Protostars and Planets VII, eds. S. Inutsuka, Y. Aikawa, T. Muto, K. Tomida, & M. Tamura, ASP Conf. Ser., 534, 379
Chaabouni, H., Diana, S., Nguyen, T., & Dulieu, F. 2018, A&A, 612, A47
Charnley, S. B. 2004, Adv. Space Res., 33, 23
Charnley, S. B., Tielens, A. G. G. M., & Millar, T. J. 1992, ApJ, 399, L71
Chen, Y., van Gelder, M. L., Nazari, P., et al. 2023, A&A, 678, A137
Chen, Y., Rocha, W. R. M., van Dishoeck, E. F., et al. 2024, A&A, 690, A205
Chuang, K. J., Fedoseev, G., Qasim, D., et al. 2020, A&A, 635, A199
Chuang, K. J., Jäger, C., Krasnokutski, S. A., Fulvio, D., & Henning, T. 2022, ApJ, 933, 107
Codella, C., Ceccarelli, C., Caselli, P., et al. 2017, A&A, 605, L3
Codella, C., Ceccarelli, C., Bianchi, E., et al. 2020, A&A, 635, A17
Coletta, A., Fontani, F., Rivilla, V. M., et al. 2020, A&A, 641, A54
Costagliola, F., Sakamoto, K., Muller, S., et al. 2015, A&A, 582, A91
Csengeri, T., Belloche, A., Bontemps, S., et al. 2019, A&A, 632, A57
Danger, G., Borget, F., Chomat, M., et al. 2011, A&A, 535, A47
Dartois, E., Chabot, M., Id Barkach, T., et al. 2019, A&A, 627, A55
Dedes, C., Leurini, S., Wyrowski, F., et al. 2011, A&A, 526, A59
de Jesus, D. N., da Silva, J. M. B. A., Tejero, T. N., et al. 2021, MNRAS, 501, 1202
De Simone, M., Codella, C., Ceccarelli, C., et al. 2020, A&A, 640, A75
Dulieu, F., Nguyen, T., Congiu, E., Baouche, S., & Taquet, V. 2019, MNRAS, 484, L119
Eibensteiner, C., Barnes, A. T., Bigiel, F., et al. 2022, A&A, 659, A173
Endres, C. P., Schlemmer, S., Schilke, P., Stutzki, J., & Müller, H. S. P. 2016, J. Mol. Spectr., 327, 95
Enrique-Romero, J., Rimola, A., Ceccarelli, C., & Balucani, N. 2016, MNRAS, 459, L6
Enrique-Romero, J., Ceccarelli, C., Rimola, A., et al. 2021, A&A, 655, A9
Enrique-Romero, J., Rimola, A., Ceccarelli, C., et al. 2022, ApJS, 259, 39
Faure, A., Lique, F., & Remijan, A. J. 2018, J. Phys. Chem. Lett., 9, 3199
Fedoseev, G., Chuang, K. J., van Dishoeck, E. F., Ioppolo, S., & Linnartz, H. 2016, MNRAS, 460, 4297
Fedoseev, G., Qasim, D., Chuang, K.-J., et al. 2022, ApJ, 924, 110
Ferrero, S., Zamirri, L., Ceccarelli, C., et al. 2020, ApJ, 904, 11
Ferrero, S., Grieco, F., Ibrahim Mohamed, A. S., et al. 2022, MNRAS, 516, 2586
Förstel, M., Bergantini, A., Maksyutenko, P., Góbi, S., & Kaiser, R. I. 2017, ApJ, 845, 83
Fuente, A., Cernicharo, J., Caselli, P., et al. 2014, A&A, 568, A65
García-Burillo, S., Martín-Pintado, J., Fuente, A., & Neri, R. 2000, A&A, 355, 499
Garrod, R. T., Widicus Weaver, S. L., & Herbst, E. 2008, ApJ, 682, 283
Garrod, R. T., Jin, M., Matis, K. A., et al. 2022, ApJS, 259, 1
Goldsmith, P. F., & Langer, W. D. 1999, ApJ, 517, 209
Golshan, R. H., Sánchez-Monge, Á., Schilke, P., et al. 2024, A&A, 688, A3
Gorai, P., Bhat, B., Sil, M., et al. 2020, ApJ, 895, 86
Gorai, P., Law, C.-Y., Tan, J. C., et al. 2024, ApJ, 960, 127
Gorski, M., Ott, J., Rand, R., et al. 2017, ApJ, 842, 124
Gorski, M. D., Ott, J., Rand, R., et al. 2019, MNRAS, 483, 5434
Gorski, M. D., Aalto, S., König, S., et al. 2023, A&A, 670, A70
Haasler, D., Rivilla, V. M., Martín, S., et al. 2022, A&A, 659, A158
Halfen, D. T., Ilyushin, V. V., & Ziurys, L. M. 2013, ApJ, 767, 66
Harada, N., Martín, S., Mangum, J. G., et al. 2021, ApJ, 923, 24
Harada, N., Martin, S., Mangum, J., et al. 2022, ApJ, 938, 80
Harada, N., Meier, D. S., Martín, S., et al. 2024, ApJS, 271, 38
Haupa, K. A., Joshi, P. R., & Lee, Y.-P. 2022, J. Chin. Chem. Soc., 69, 1159
Henkel, C., Jacq, T., Mauersberger, R., Menten, K. M., & Steppe, H. 1987, A&A, 188, L1
Herbst, E., & van Dishoeck, E. F. 2009, ARA&A, 47, 427

Holdship, J., Viti, S., Codella, C., et al. 2019, ApJ, 880, 138
Holdship, J., Mangum, J. G., Viti, S., et al. 2022, ApJ, 931, 89
Huang, K.-Y., Viti, S., Holdship, J., et al. 2023, A&A, 675, A151
Huang, K. Y., Abbink, D., Viti, S., & García-Burillo, S. 2024, A&A, 688, A130
Huang, K. Y., Behrens, E., Bouvier, M., et al. 2025, A&A, submitted
Humire, P. K., Thiel, V., Henkel, C., et al. 2020, A&A, 642, A222
Humire, P. K., Henkel, C., Hernández-Gómez, A., et al. 2022, A&A, 663, A33
Ibrahim, M., Guillemin, J.-C., Chaquin, P., Markovits, A., & Krim, L. 2022, Physical Chemistry Chemical Physics (Incorporating Faraday Transactions), 24, 23245
Iodice, E., Arnaboldi, M., Rejkuba, M., et al. 2014, A&A, 567, A86
Jimenez-Serra, I. 2025, ArXiv e-prints [arXiv:2501.01782]
Jin, M., & Garrod, R. T. 2020, ApJS, 249, 26
Jones, P. A., Burton, M. G., Tothill, N. F. H., & Cunningham, M. R. 2011, MNRAS, 411, 2293
Jørgensen, J. K., Müller, H. S. P., Calcutt, H., et al. 2018, A&A, 620, A170
Jørgensen, J. K., Belloche, A., & Garrod, R. T. 2020, ARA&A, 58, 727
Kahane, C., Ceccarelli, C., Faure, A., & Caux, E. 2013, ApJ, 763, L38
Kim, Y. S., & Kaiser, R. I. 2011, ApJ, 729, 68
Kishikawa, R., Harada, N., Saito, T., et al. 2025, PASJ, 77, 1
Krieger, N., Bolatto, A. D., Leroy, A. K., et al. 2020, ApJ, 897, 176
Kurtz, S., Cesaroni, R., Churchwell, E., Hofner, P., & Walmsley, C. M. 2000, in Protostars and Planets IV, eds. V. Mannings, A. P. Boss, & S. S. Russell, 299
Lamberts, T., Markmeyer, M. N., Kolb, F. J., & Kästner, J. 2019, ACS Earth Space Chem., 3, 958
Lee, C.-F., Codella, C., Li, Z.-Y., & Liu, S.-Y. 2019, ApJ, 876, 63
Lefloch, B., Ceccarelli, C., Codella, C., et al. 2017, MNRAS, 469, L73
Leroy, A. K., Bolatto, A. D., Ostriker, E. C., et al. 2015, ApJ, 801, 25
Leroy, A. K., Bolatto, A. D., Ostriker, E. C., et al. 2018, ApJ, 869, 126
Levy, R. C., Bolatto, A. D., Leroy, A. K., et al. 2021, ApJ, 912, 4
Li, C., Qin, S.-L., Liu, T., et al. 2024, MNRAS, 533, 1583
Li, J., Shen, Z., Wang, J., et al. 2017, ApJ, 849, 115
Li, J., Wang, J., Qiao, H., et al. 2020, MNRAS, 492, 556
Ligterink, N. F. W., Terwisscha van Scheltinga, J., Taquet, V., et al. 2018, MNRAS, 480, 3628
López-Sepulcre, A., Jaber, A. A., Mendoza, E., et al. 2015, MNRAS, 449, 2438
López-Sepulcre, A., Balucani, N., Ceccarelli, C., et al. 2019, ACS Earth Space Chem., 3, 2122
López-Sepulcre, A., Codella, C., Ceccarelli, C., Podio, L., & Robuschi, J. 2024, A&A, 692, A120
Lu, Y., Quan, D., Chang, Q., Chen, L.-F., & Li, D. 2025, ApJS, 277, 8
Mangum, J. G., Ginsburg, A. G., Henkel, C., et al. 2019, ApJ, 871, 170
Maret, S., Hily-Blant, P., Pety, J., Bardeau, S., & Reynier, E. 2011, A&A, 526, A47
Martín, S., Mauersberger, R., Martín-Pintado, J., Henkel, C., & García-Burillo, S. 2006, ApJS, 164, 450
Martín, S., Krips, M., Martín-Pintado, J., et al. 2011, A&A, 527, A36
Martín-Doménech, R., Öberg, K. I., & Rajappan, M. 2020, ApJ, 894, 98
Martín, S., Mangum, J. G., Harada, N., et al. 2021, A&A, 656, A46
Matthews, H. E., Friberg, P., & Irvine, W. M. 1985, ApJ, 290, 609
Mauersberger, R., Henkel, C., Walmsley, C. M., Sage, L. J., & Wiklind, T. 1991, A&A, 247, 307
McCarthy, P. J., van Breugel, W., & Heckman, T. 1987, AJ, 93, 264
McCormick, A., Veilleux, S., & Rupke, D. S. N. 2013, ApJ, 774, 126
Meier, D. S., Walter, F., Bolatto, A. D., et al. 2015, ApJ, 801, 63
Mills, E. A. C., Gorski, M., Emig, K. L., et al. 2021, ApJ, 919, 105
Mininni, C., Beltrán, M. T., Colzi, L., et al. 2023, A&A, 677, A15
Möller, T., Schilke, P., Sánchez-Monge, Á., & Schmiedeke, A. 2025, A&A, 693, A160
Molpeceres, G., Kästner, J., Herrero, V. J., Peláez, R. J., & Maté, B. 2022, A&A, 664, A169
Molpeceres, G., Furuya, K., & Aikawa, Y. 2024a, A&A, 688, A150
Molpeceres, G., Tsuge, M., Furuya, K., Watanabe, N., et al. 2024b, J. Phys. Chem. A, 128, 3874
Müller, H. S. P., Schlöder, F., Stutzki, J., & Winnewisser, G. 2005, JMoSt, 742, 215
Muller, S., Beelen, A., Guélin, M., et al. 2011, A&A, 535, A103
Muller, S., Ubachs, W., Menten, K. M., Henkel, C., & Kanekar, N. 2021, A&A, 652, A5
Müller-Sánchez, F., González-Martín, O., Fernández-Ontiveros, J. A., Acosta-Pulido, J. A., & Prieto, M. A. 2010, ApJ, 716, 1166
Nazari, P., Meijerhof, J. D., van Gelder, M. L., et al. 2022, A&A, 668, A109
Osterbrock, D. E. 1974, Astrophysics of Gaseous Nebulae (San Franciso: Freeman), A Series of Books in Astronomy and Astrophysics
Paulive, A., Carder, J. T., & Herbst, E. 2022, MNRAS, 516, 4097
Pearson, J. C., Brauer, C. S., & Drouin, B. J. 2008, J. Mol. Spectr., 251, 394
Peng, Y., Liu, T., Qin, S.-L., et al. 2022, MNRAS, 512, 4419

Perrero, J., Enrique-Romero, J., Martínez-Bachs, B., et al. 2022, ACS Earth and Space Chemistry, 6, 496

Perrero, J., Vitorino, J., Congiu, E., et al. 2024, Physical Chemistry Chemical Physics (Incorporating Faraday Transactions), 26, 18205

Pickett, H. M., Poynter, R. L., Cohen, E. A., et al. 1998, JQSRT, 60, 883

Pérez-Beaupuits, J. P., Güsten, R., Harris, A., et al. 2018, ApJ, 860, 23

Qiu, J., Wang, J., Shi, Y., et al. 2018, A&A, 613, A3

Quénard, D., Jiménez-Serra, I., Viti, S., Holdship, J., & Coutens, A. 2018, MNRAS, 474, 2796

Raunier, S., Chiavassa, T., Duvernay, F., et al. 2004, A&A, 416, 165

Rekola, R., Richer, M. G., McCall, M. L., et al. 2005, MNRAS, 361, 330

Requena-Torres, M. A., Martín-Pintado, J., Rodríguez-Franco, A., et al. 2006, A&A, 455, 971

Rico-Villas, F., Martin-Pintado, J., Gonzalez-Alfonso, E., Martin, S., & Rivilla, V. M. 2020, MNRAS, 491, 4573

Rimola, A., Skouteris, D., Balucani, N., et al. 2018, ACS Earth Space Chem., 2, 720

Rivilla, V. M., García De La Concepción, J., Jiménez-Serra, I., et al. 2022a, Front. Astron. Space Sci., 9, 829288

Rivilla, V. M., Jiménez-Serra, I., Martín-Pintado, J., et al. 2022b, Front. Astron. Space Sci., 9, 876870P

Roberts, J. F., Rawlings, J. M. C., Viti, S., & Williams, D. A. 2007, MNRAS, 382, 733

Rocha, W. R. M., van Dishoeck, E. F., Ressler, M. E., et al. 2024, A&A, 683, A124

Rodríguez-Rico, C. A., Goss, W. M., Zhao, J. H., Gómez, Y., & Anantharamaiah, K. R. 2006, ApJ, 644, 914

Rosenberg, M. J. F., Kazandjian, M. V., van der Werf, P. P., et al. 2014, A&A, 564, A126

Ruaud, M., Loison, J. C., Hickson, K. M., et al. 2015, MNRAS, 447, 4004

Rubin, M., Altwegg, K., Balsiger, H., et al. 2019, MNRAS, 489, 594

Sakamoto, K., Mao, R.-Q., Matsushita, S., et al. 2011, ApJ, 735, 19

Sanz-Novo, M., Rivilla, V. M., Jiménez-Serra, I., et al. 2024, ApJ, 965, 149

Sewiło, M., Indebetouw, R., Charnley, S. B., et al. 2018, ApJ, 853, L19

Shimonishi, T., Tanaka, K. E. I., Zhang, Y., & Furuya, K. 2023, ApJ, 946, L41

Sil, M., Gorai, P., Das, A., et al. 2018, ApJ, 853, 139

Sivaramakrishnan, R., Su, M.-C., Michael, J. V., et al. 2009, J. Phys. Chem., A, 114, 755

Skouteris, D., Vazart, F., Ceccarelli, C., et al. 2017, MNRAS, 468, L1

Skouteris, D., Balucani, N., Ceccarelli, C., et al. 2018, ApJ, 854, 135

Suzuki, T., Ohishi, M., Hirota, T., et al. 2016, ApJ, 825, 79

Suzuki, T., Ohishi, M., Saito, M., et al. 2018, ApJS, 237, 3

Suzuki, T., Majumdar, L., Goldsmith, P. F., et al. 2023, ApJ, 954, 189

Tanaka, K., Mangum, J. G., Viti, S., et al. 2024, ApJ, 961, 18

Tercero, B., Cuadrado, S., López, A., et al. 2018, A&A, 620, L6

Theule, P., Borget, F., Mispelaer, F., et al. 2011, A&A, 534, A64

Turner, B. E., Terzieva, R., & Herbst, E. 1999, ApJ, 518, 699

Ulvestad, J. S., & Antonucci, R. R. J. 1997, ApJ, 488, 621

Urso, R. G., Scirè, C., Baratta, G. A., et al. 2017, Physical Chemistry Chemical Physics (Incorporating Faraday Transactions), 19, 21759

van der Walt, S. J., Kristensen, L. E., Jørgensen, J., et al. 2021, A&A, 655, A86

Vasyunin, A. I., & Herbst, E. 2013, ApJ, 769, 34

Vazart, F., Calderini, D., Puzzarini, C., Skouteris, D., & Barone, V. 2016, J. Chem. Theory Comput., 12, 5385

Vazart, F., Ceccarelli, C., Balucani, N., Bianchi, E., & Skouteris, D. 2020, MNRAS, 499, 5547

Viti, S., Collings, M. P., Dever, J. W., McCoustra, M. R. S., & Williams, D. A. 2004, MNRAS, 354, 1141

Widicus Weaver, S. L., Laas, J. C., Zou, L., et al. 2017, ApJS, 232, 3

Woon, D. E. 2002, ApJ, 571, L177

Xue, C., Remijan, A., Faure, A., et al. 2024, ApJ, 967, 164

Yamamoto, S. 2017, Introduction to Astrochemsitry: chemical Evolution from Interstellar Clouds to Star and Planet Formation (New York: Springer)

Yang, Y.-L., Sakai, N., Zhang, Y., et al. 2021, ApJ, 910, 20

Zeng, S., Jiménez-Serra, I., Rivilla, V. M., et al. 2018, MNRAS, 478, 2962

Zeng, S., Zhang, Q., Jiménez-Serra, I., et al. 2020, MNRAS, 497, 4896

Appendix A: Integrated intensity images

The velocity integrated maps for CH_3NH_2, CH_2NH, CH_3CHO, NH_2CHO, and C_2H_5OH, are presented here. The velocities used for the integration are within the range 70-380 km s^{-1}.
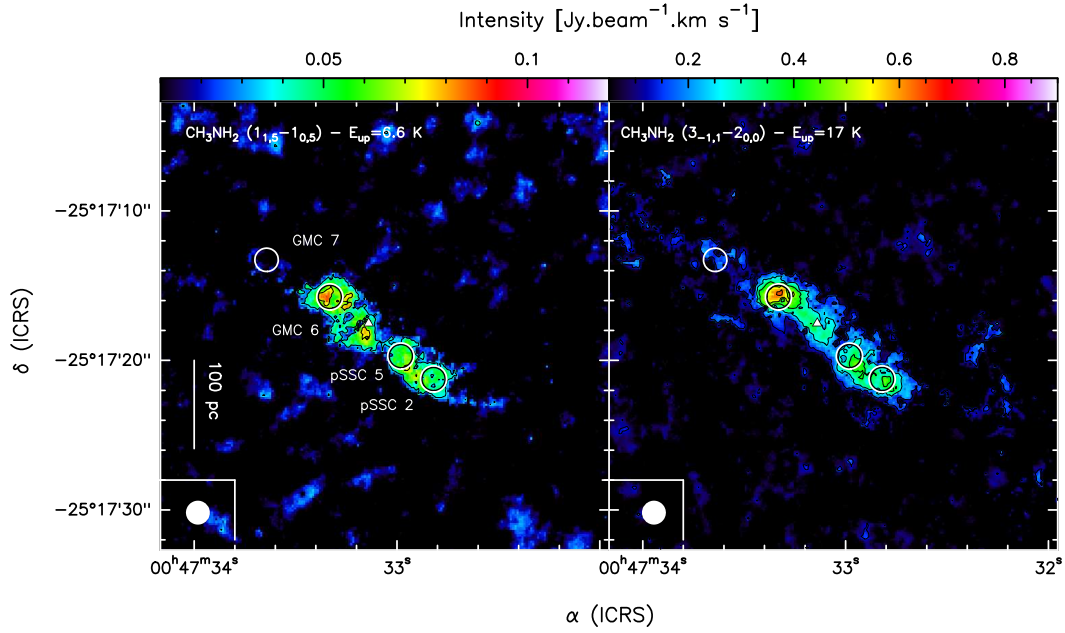

Fig. A.1. Velocity-integrated images of CH_3NH_2. The kinematic centre (Müller-Sánchez et al. 2010) is labelled by a white triangle. The regions where the spectra were extracted are shown by the black and white circles and are labelled in the left-most panel. The beam is depicted in the lower left corner of each plot. The scale bar of 100 pc corresponds to ~6″. *Left:* Velocity-integrated map of CH_3NH_2 ($1_{1,5} - 1_{0,5}$). Levels start at 3σ (1σ =42 mJy beam^{-1} km s^{-1}) with steps of 3σ. *Right:* Velocity-integrated map of CH_3NH_2 ($3_{-1,1} - 2_{0,0}$). Levels start at 3σ (1σ =42 mJy beam^{-1} km s^{-1}) with steps of 3σ.
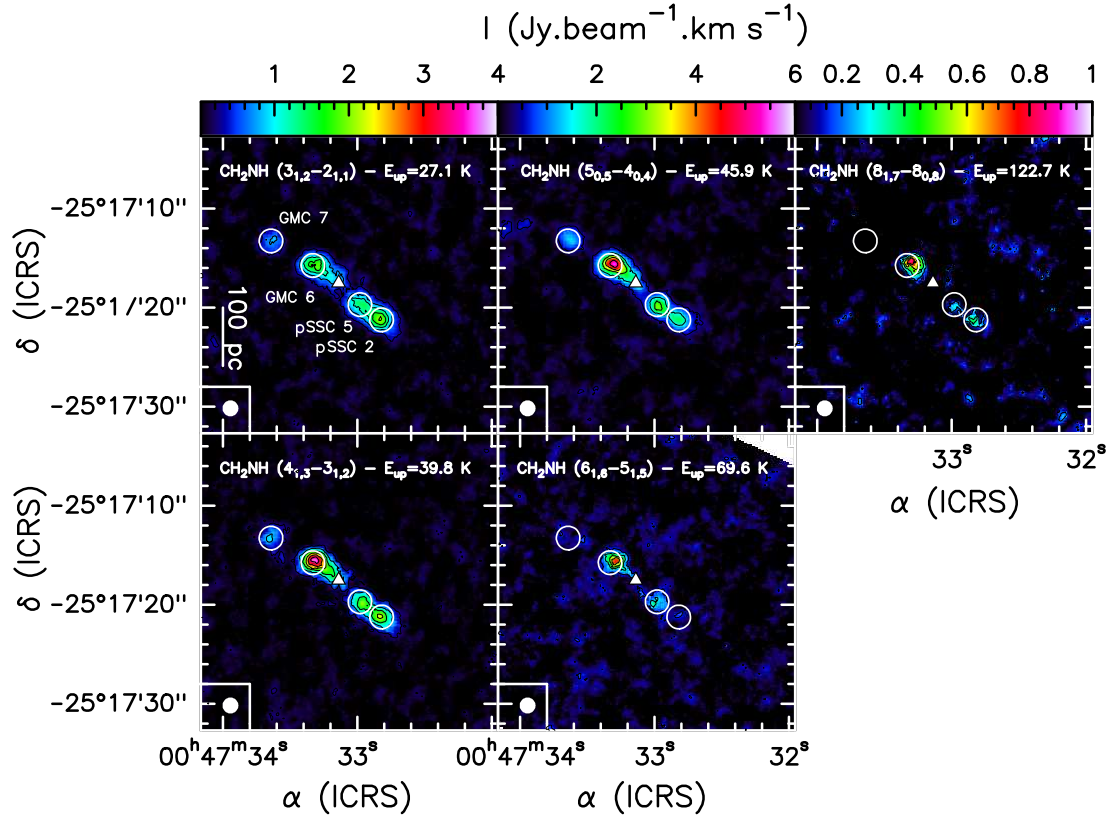
Fig. A.2. Same as Figure A.1 but for CH₂NH. *Top Left:* Velocity-integrated map of CH₂NH ($3_{1,2} - 2_{1,1}$). Levels start at 3σ ($1\sigma = 90\,\mathrm{mJy\,beam^{-1}\,km\,s^{-1}}$) with steps of 5σ. *Bottom Left:* Velocity-integrated map of CH₂NH ($4_{1,3} - 3_{1,2}$). Levels start at 3σ ($1\sigma = 78\,\mathrm{mJy\,beam^{-1}\,km\,s^{-1}}$) with steps of 8σ. *Middle Top:* Velocity-integrated map of CH₂NH ($5_{0,5} - 4_{0,4}$). Levels start at 3σ ($1\sigma = 140\,\mathrm{mJy\,beam^{-1}\,km\,s^{-1}}$) with steps of 8σ. *Bottom Middle:* Velocity-integrated map of CH₂NH ($6_{1,6} - 5_{1,5}$). Levels start at 3σ ($1\sigma = 210\,\mathrm{mJy\,beam^{-1}\,km\,s^{-1}}$) with steps of 5σ. *Top Right:* Velocity-integrated map of CH₂NH ($8_{1,7} - 8_{0,8}$). Levels start at 3σ ($1\sigma = 61\,\mathrm{mJy\,beam^{-1}\,km\,s^{-1}}$) with steps of 3σ.
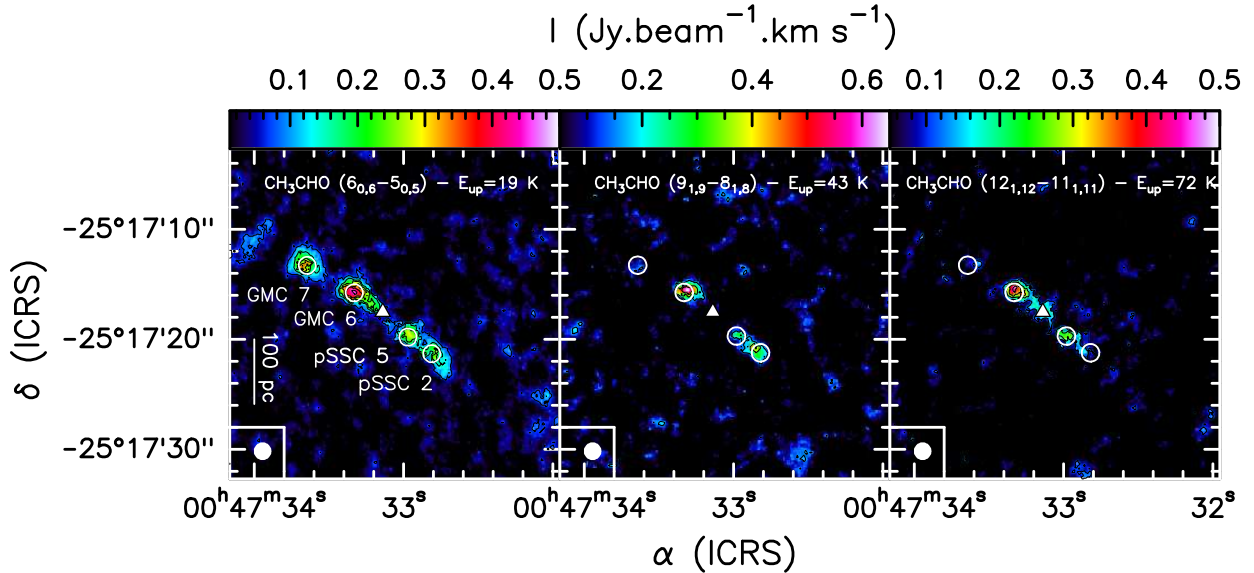

Fig. A.3. Same as Figure A.1 but for CH₃CHO. *Left:* Velocity-integrated map of CH₃CHO ($1_{1,5} - 1_{0,5}$ (E+A)). Levels start at 3σ ($1\sigma = 25\,\mathrm{mJy\,beam^{-1}\,km\,s^{-1}}$) with steps of 3σ. *Middle:* Velocity-integrated map of CH₃CHO ($9_{2,9} - 8_{1,8}$ (E+A)). Levels start at 3σ ($1\sigma = 55\,\mathrm{mJy\,beam^{-1}\,km\,s^{-1}}$) with steps of 3σ. *Right:* Velocity-integrated map of CH₃CHO ($12_{1,12} - 11_{1,11}$ (E+A)). Levels start at 3σ ($1\sigma = 36\,\mathrm{mJy\,beam^{-1}\,km\,s^{-1}}$) with steps of 3σ.
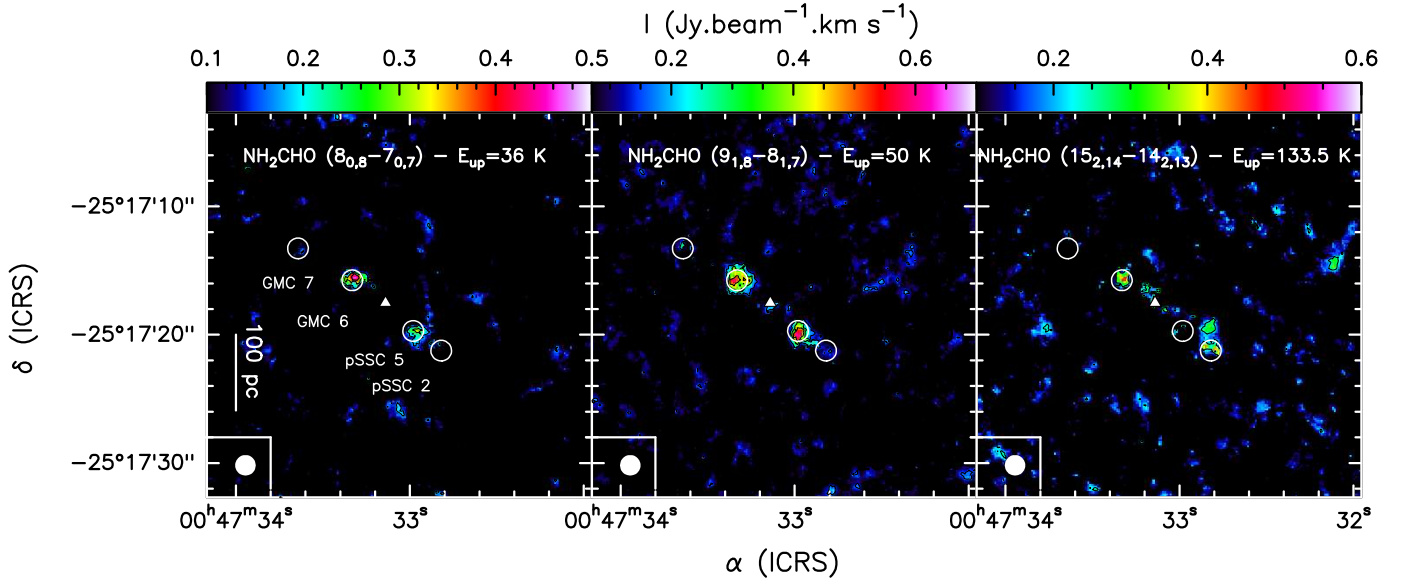
Fig. A.4. Same as Figure A.1 but for NH$_2$CHO. *Left:* Velocity-integrated map of NH$_2$CHO ($8_{0,8} - 7_{0,7}$). Levels start at 3σ ($1\sigma = 58$ mJy beam^{-1} km s^{-1}) with steps of 2σ. *Middle:* Velocity-integrated map of NH$_2$CHO ($9_{1,8} - 8_{1,7}$). Levels start at 3σ ($1\sigma = 52$ mJy beam^{-1} km s^{-1}) with steps of 3σ. *Right:* Velocity-integrated map of NH$_2$CHO ($15_{2,14} - 14_{2,13}$). Levels start at 3σ ($1\sigma = 78$ mJy beam^{-1} km s^{-1}) with steps of 3σ.
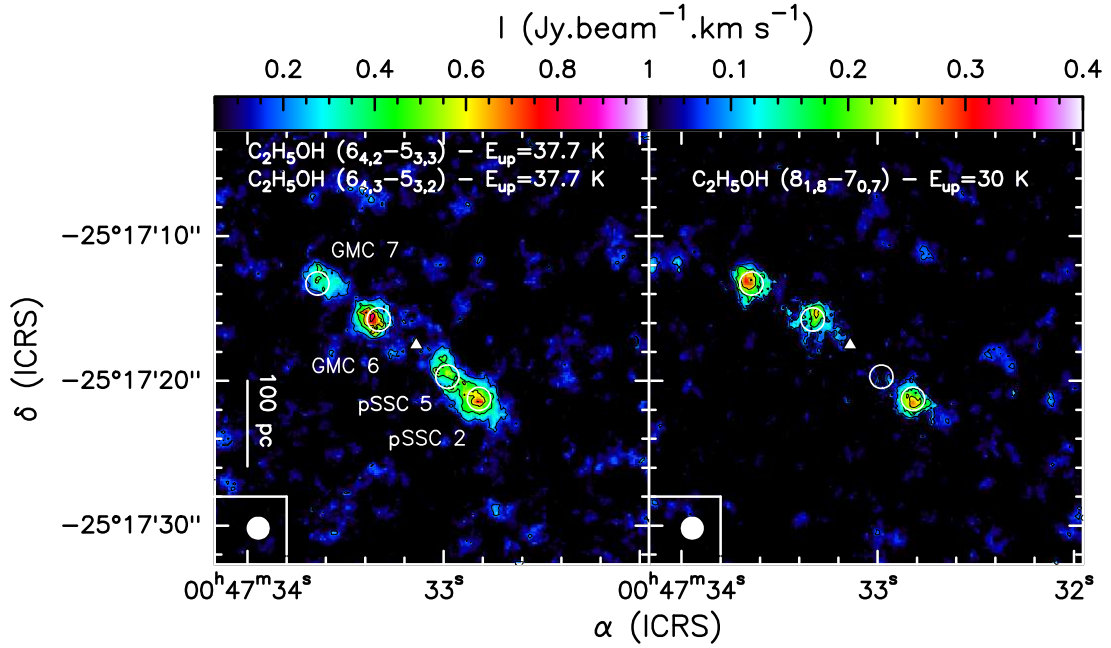

Fig. A.5. Same as Figure A.1 but for t-C$_2$H$_5$OH. *Left:* Velocity-integrated map of t-C$_2$H$_5$OH ($6_{4,2} - 5_{3,3}$ and $6_{4,3} - 5_{3,2}$; blended together). Levels start at 3σ ($1\sigma = 64$ mJy beam^{-1} km s^{-1}) with steps of 3σ. *Right:* Velocity-integrated map of t-C$_2$H$_5$OH ($8_{1,8} - 7_{0,7}$). Levels start at 3σ ($1\sigma = 26$ mJy beam^{-1} km s^{-1}) with steps of 3σ.